

COGEAR

MODULE 3:

Generic studies on soil slope dynamics

Del. No.: 3b.3.4

Authors: Dupray F., Chao L., and Laloui, L.

Laboratory of Soil Mechanics, EPFL

July 12, 2012

ENAC - Faculté Environnement naturel, architectural et construit
LMS - Laboratoire de mécanique des sols

EPFL - LMS
Station 18
CH - 1015 Lausanne

Tél.: +41 (0)21 693 23 15
Fax: +41 (0)21 693 41 53
Web: <http://lms.epfl.ch>



Competence Center Environment and Sustainability

COGEAR: COupled seismogenic GEohazards in Alpine Regions

MODULE 3 – Deliverable 3b.3.4

Generic studies on soil slope dynamics

Authors: Dr F. Dupray, L. Chao, Prof. L. Laloui

Summary

INTRODUCTION.....	3
1 Landslides and earthquakes in Valais.....	4
1.1 Main features about <i>Les Peillettes</i>	4
1.1.1 Geological and tectonic information	6
1.1.2 Hydrology information.....	6
1.1.3 Graphical interpretation.....	7
2 Requirement and selection of software	9
3 Geo-mechanical model.....	10
3.1 Hujeux-ECP 1985 model.....	10
3.1.1 Notations	10
3.1.2 Elasticity	11
3.1.3 Deviatoric mechanisms	11
3.1.4 Isotropic mechanisms	14
3.1.5 Interpretation of ECP-Hujeux model.....	15
3.2 Governing equations for poroelastic media.....	17
3.2.1 Application domains.....	18
3.3 Paraxial element	19
4 Dynamic analysis for <i>Les Peillettes</i>	22
4.1 Elementary test.....	22
4.2 Finite element model	25
4.3 Response to the earthquake	27
Conclusion.....	35
References	36

INTRODUCTION

In Switzerland, past earthquakes are known to have triggered landslides of various natures (rock, soil) and various importances. An earthquake with a magnitude of 6.1 in the region of Sierre in 1946 destroyed 412 chimneys, caused numerous injuries and triggered large the Six des Eaux-froides rockfall. One of the aftershocks triggered a landslide of 4 to 5 million cubic meters on the slopes of the Rawylhorn which in turn caused main damages. On July 25th, 1855, between Visp and Saint Niklaus a small village was subjected an earthquake with an estimated magnitude of 6.4, only one building remained undamaged.

Swiss Seismological Service underlined in the report Seismic hazard assessment of Switzerland (Giardini et al. 2004) that the region in the Rhone Valais will continue being a very seismically active zone in the future. Landslides are identified as one of the major hazards in the Rhone Valais. Several landslides were observed during history in Valais.

The study of soil slope dynamics can be performed by two distinct methods. The first method is a semi-probabilistic approach that uses simple simulations and many seisms as input to estimate the probability of failure (Arvin *et al.* 2012). The second is the deterministic approach, which was selected for that part of the project. It involves studying a possible local event for the input (synthetic ground motion or actual previous event) and combining it with a deterministic study. Such an advanced study can be separated in three aspects. The first aspect is the non-linear response of the soil, in an inclined situation. This can be assessed through 1D simulations, which are reported in a separate report dedicated to the Grächen site, numbered 3b.3.6.1. The second aspect is the effect of the geometry of the considered place, which is tackled in another report, numbered 3b.3.7.1. The final aspect is to study the possibility of predicting how an active soil slope will react to the coupled hazard of a seism, and this is the part that is studied in this report.

The mechanisms that govern triggering and sliding of landslides in such cases are not well-known. The topic is difficult to explore because of both the nature of earthquake motion and the dynamic characteristics of the soil. In addition, geology, morphology, heterogeneity in soils and site effects are believed to have an influence on the possible slide-triggering. In order to focus these studies on the specific case of Valais, a generic case study has been selected among active landslides in Valais, as the *Les Peillettes* landslide in the commune of Grône. The goals are to assess whether a simulation is capable of identifying the main kind of landslide that could be triggered, such as a shallow or deep-seated landslide, and also to estimate the response of a typical landslide, in terms of site effect.

This report is divided into three main parts. The first part reminds how comparable situations can be treated in the literature; the second describes general information about *Les Peillettes* such as geometry, geology and drilling borehole information, which is followed by several important theories of different aspects concerning soil dynamics. Finally, a two-dimensional analysis is presented to focus on soil behaviour and evaluation of numerical model.

1 Landslides and earthquakes in Valais

The region of Valais is the largest seismically active region in Switzerland. The Valais experiences an earthquake with a magnitude 6 or above every 100 years according to a probabilistic study by Fritsche *et al.* (2010).

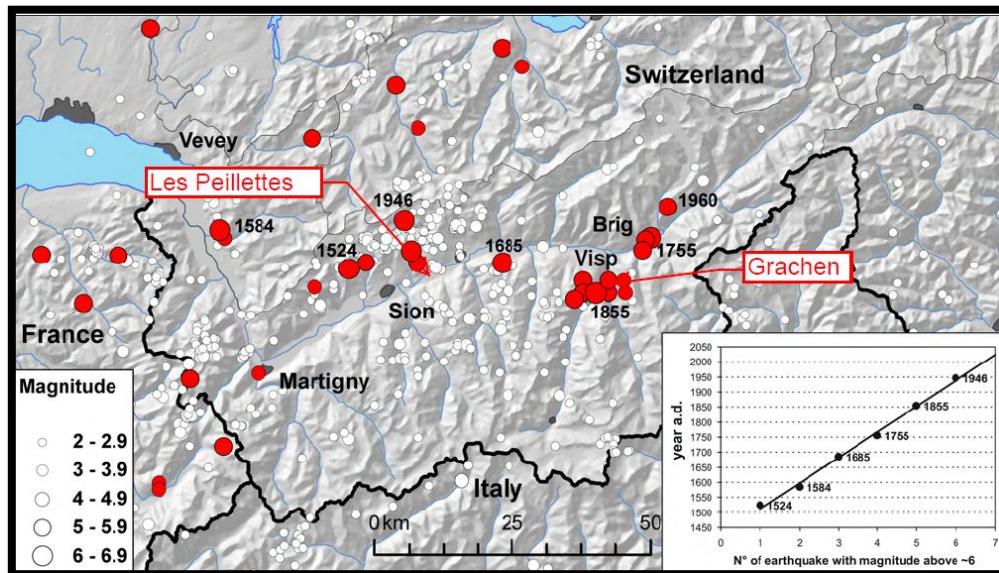


Figure 1: Large earthquakes in the Valais and the timing of magnitude 6 or larger historical events. (Fäh and COGEAR Working Group 2010)

On July 25th, 1855, an earthquake of almost VIII intensity, with a magnitude estimated at 6.4 occurred in the region close to Grächen. Between Visp and St Niklaus, only one building remained up. On January 25th, 1946, in the region of Sierre, on the west of *Les Peillettes*, a magnitude 6.1 earthquake occurred with maximum intensity VIII, which damaged about 4000 buildings at various levels. On May 30th in the same year, an aftershock with an intensity of VII triggered a landslide of 4 to 5 million cubic meters nearby.

These areas experience damages not only from ground motion alone but also secondary effects such as triggered landslides, soil liquefaction and rock falls. A small scale seismic and frequent shaking could provoke failures in steep slopes. Furthermore it will reduce soil strength and could influence the stability of a landslide in the long-term, which is also a critical question for the studied areas.

These questions need to be addressed at the generic scale in this report, and therefore the choice of an active and relatively well-known landslide is deemed necessary for this task. The chosen landslide, *Les Peillettes*, has interesting characteristics in that its mechanisms are understood: the superficial debris flow is linked with a steep slope and water accumulation, while the larger movement is linked with a rise in the water table and a weak zone in a slightly less steep area.

1.1 Main features about *Les Peillettes*

Les Peillettes is a historically famous landslide where a large landslide happened in 1980. Since then, although mitigating measures have been taken, the landslide remains active, with the additional risk of debris flow in the Grand-Tsâble area. The area is known as a zone of seismic activity, which led to the

question of evaluating the risk associated with the combination of a landslide and a seism. The usual triggering mechanism for this landslide is heavy rainfall or a rise in water table through snow melting, but the goal is to study possible coupled hazard scenarios including the effect of an earthquake.

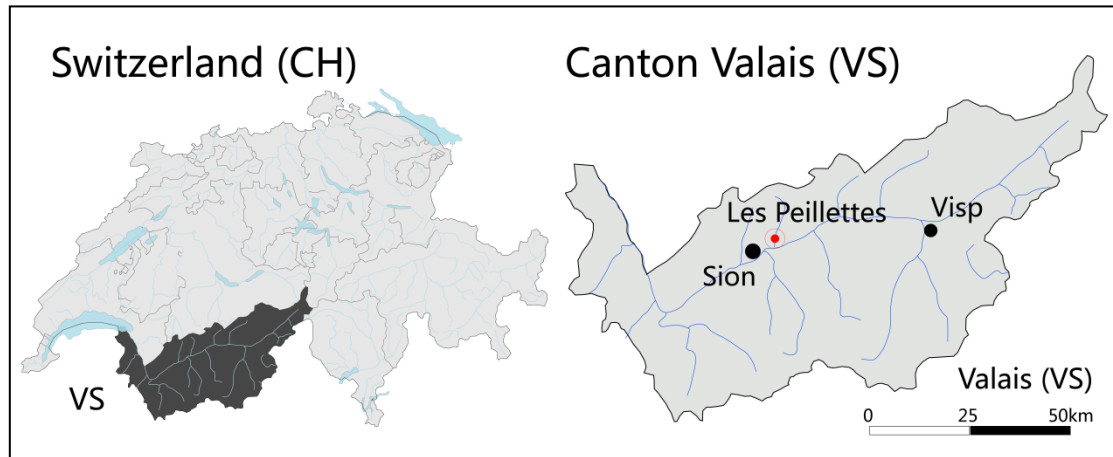


Figure 2: Location of landslide Les Peillettes in the canton of Valais, Switzerland

The general information about hydrology and geology of Peillettes in this section is largely summarized from the report *Glissement des Peillettes – Rapport campagne de forages profonds* (Bianchetti and Bagnoud 1999).

The landslide named *Les Peillettes* is situated at the left hand of Rhône valley, above the village of Grône and between the towns of Sion and Siere (Cf. Figure 2). It is one of the largest landslides in the Valais with about 1.3 km² instable zone and is located at altitudes between 950 m a.s.l. and 2050 m a.s.l.

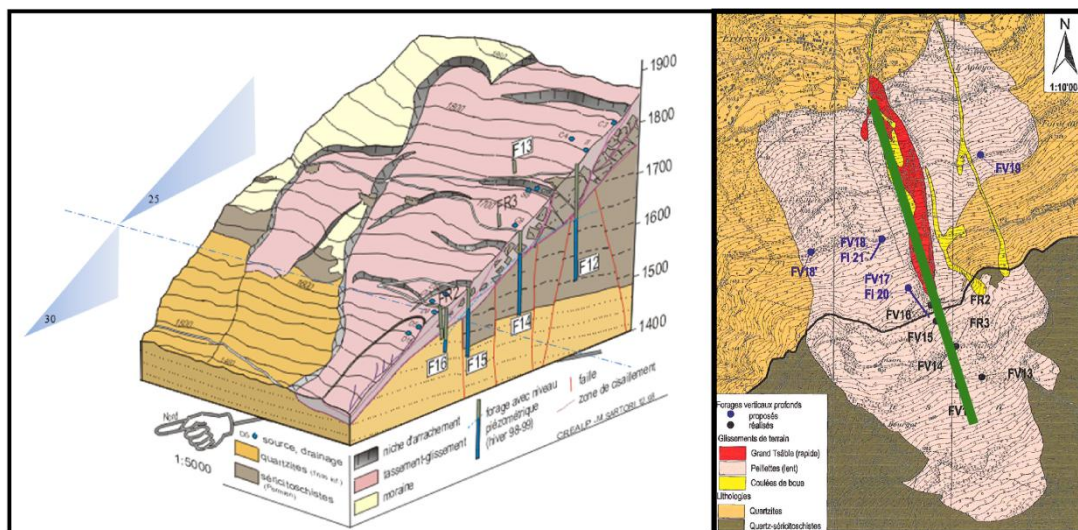


Figure 3: (left) 3D geology plan of Les Peillettes. (right) Borehole map of landslide Grand-Tsâble and Les Peillettes. (green line: location of the studied cross section) (Bianchetti and Bagnoud 1999).

In the centre of the large moving mass, a shallow (ca. 10 m) more active landslide which is called “Grand-Tsâble” exists (cf. red zone in Figure 3). This slope is about 0.1 km² spreading from the top of its niche (1600 m a.s.l.) to the foot of *Peillettes* landslide (1000 m a.s.l.) directly above the local village. Its nature is different, more akin to a debris flow that can be activated by extreme rainfall. This landslide in a landslide is composed of a compact and fine mass with sericite schist blocks whose volume can reach 5 m³ and above.

1.1.1 Geological and tectonic information

The bedrock of *Les Peillettes* is made of quartz-sericite-schist, fissured and resistant quartz, on top of Triassic quartz. The general fracture orientation is from east to west, perpendicular to the direction of the landslide. The slopes result from the alterations of the schist on surface of bedrock, and also from the mobilization of moraine deposits. Shallower material is also formed of rocky blocks packed by silt-alluvium mixed clays. The size of these blocks decreases gradually towards the surface of the slope. It should be noted from the 3D geology atlas (Figure 3) that a change of slope angle from 25 degrees to 30 degrees occurs at the altitude of 1590m a.s.l. where it coincides with a lithological change, schist to quartz. In addition, this is also the slide surface which started the Grand-Tsâble landslide.

Sixteen boreholes provide more information about soil material above the bedrock. Borehole locations can be seen on Figure 4. Borehole FV16 represents a soil section with depth of 85m. First 43 meters are made up of a dry layer of silty clay with an abundance of gravel, without rock fragments. Next 5 meter layer is recognized as slide surface with a wet layer of silt and clay. This borehole end when it meets a layer of very cracked rock. Water can dissipate easily in this zone.

In the borehole FV15, the first 27 meters have a layer of silty clay, gravel and no rock fragments, which is the same as the first layer in FV16. The following 3 meters are also recognized as a slip plan with only wet clay. Below the slip plan exists a layer with gravel and silty clay, with angular rock fragments. This layer rests on the bedrock made up of a saturated zone of Permian quartz rock.

The other 2 boreholes FV12 and FV14 provide more or less the same information. A 30 meter deep layer contains silty clay and gravel. The following layer containing the rock angular fragments has a depth of 50 meters in FV12 and 25 meters in FV14.

All the layers above the bedrock consist of the body of landslide of *Les Peillettes*. Due to the complexity of their nature and their fine material content, these materials can be handled as soils with a non-linear behaviour. The presence of blocks, however, should be kept in mind and some phenomena that are known to happen in some uniform soils, such as liquefaction, cannot be expected here.

1.1.2 Hydrology information

Main cause of landslide of *Les Peillettes* from the history was the infiltration and the resultant transient changes in the hydrological systems. A borehole investigation has been conducted by CREALP started from 1997. Results of 5 boreholes (FV12 to FV16) installed on the uphill of Grand Tsâble as shown in Figure 3 are summarized by the Table 1.

Extreme positions of water table identified in boreholes are not significantly different. The aquifer is almost stable during 1998-1999. For an earthquake analysis, during a very short period of about 20 seconds, we can assume that the water table is constant during seismic loading. The water level measured by boreholes is generally situated 3-5 meters above bedrock.

Borehole No.	FV12	FV13	FV14	FV15	FV16
Installation date (mm.yy)	11.97	12.97 & 05.98	06.98	07.98	08.98
Coordinate	603°027/119°9 72	603°125/120°0 06	603°006/120°1 29	602°932/120°2 41	602°909/120°3 08
Altitude [a.s.l.]	1751.88	1747.75	1683.70	1622.28	1594.85
Length [m]	178	181.5	158	129	86
Landslide Layer[m]	0-75	0-70	0-52.5	0-54	0-48
Quartz-sericite-schist Layer [m]	75-178	70-181.5	52.5-155	54-112	-
Quartz Layer [m]	-	-	From 155	From 112	From 48
Flow velocity	113-128m (135 l/min)	85-93m (100 l/min)	50m (25 l/min)	37m (20 l/min)	25m (20 l/min)
Cumulative flow	-	123-144m (100 l/min)	95-100m (20 l/min)	65-80m (100 l/min)	-
	-	157-174m (280 l/min)	115-127m (100 l/min)	91-104m (80 l/min)	-
Highest water level (dd.mm.yy)	89.86m (18.12.97)	86.40m (07.07.98)	43.06m (06.12.98)	37.86m (04.12.98)	67.84m (24.03.99)
Lowest water level (dd.mm.yy)	91.54m (24.03.99)	87.49m (24.03.99)	43.20m (24.03.99)	38.28m (07.09.98)	71.86m (08.09.98)
Mean temperature (°)	3.6	4.1	3.9	4.2	4.3

Table 1: Summary of borehole information

1.1.3 Graphical interpretation

The cross section used in dynamic simulation is the one that we can see from right in 3D geology plan (Figure 3). Details about this section are shown in the Figure 4 in order to better represent the geology and hydrology information.

Two parts are identified with separate characteristics: the Grand-Tsâble surface landslide and the less steep area above it which shows more complexity in its behaviour. The interesting zone consists of two major soil covers. Cover #1 has no blocks in its body, which is opposite to soil cover #2. Slide surface is situated at the uphill head of the landslide Grand-Tsâble.

Water table is situated in the soil cover #2 and above the Permian quartz. Since the Trias quartz is very cracked, water can dissipate very easily in this layer, pore water pressure therefore is assumed to be zero in this zone.

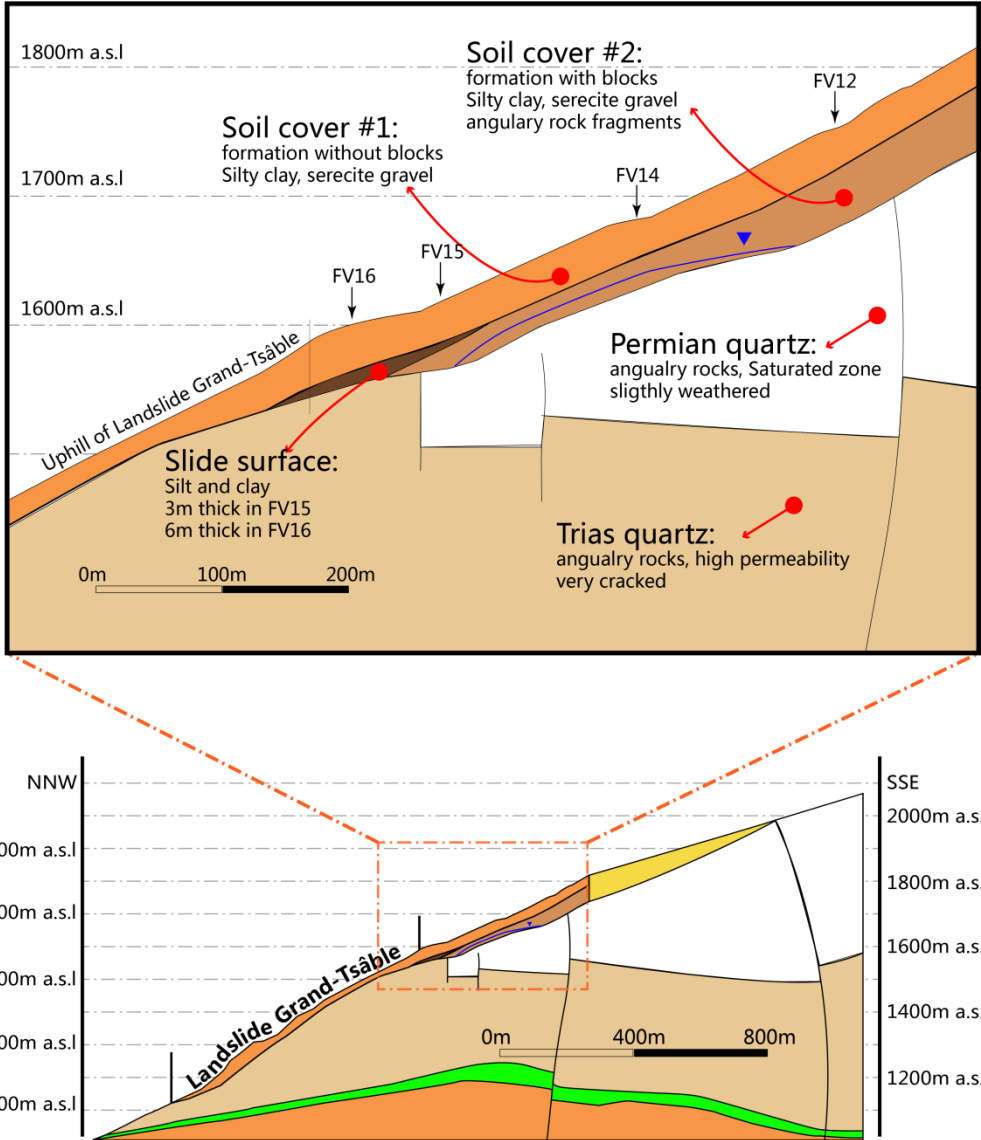


Figure 4: Detailed cross section for this study. The zone of main interest is zoomed.

2 Requirement and selection of software

In order to simulate soil behaviour, an appropriate application needs to be selected according to specific requirements for the study. In the case of a dynamic analysis, not only constitutive laws for dynamic loading should be taken into account, but also the capacity to simulate the boundary conditions in a seismic event should be paid attention. Seismic waves will be reflected by artificial boundaries if they are not designed for seismic analysis, which would lead to an over-estimation of site response.

Such tool for complete dynamic simulation exists but its complexity, and the need for detailed data, makes it of rare use. Simulations for *Les Peillettes* are performed by the finite element code *GefDyn* (Aubry et al. 1986). This code allows for bi- and tri-dimensional static and dynamic analysis, which takes into account the nonlinearity of soil, a hydro-mechanic coupled formulation and is capable to model static and dynamic loadings. In addition it is the sole code that can take into account the Hujieux model for dynamic calculation with special elements to solve boundary problems.

From literature, several researches about landslides were conducted for different aspects using *GefDyn*. Laloui *et al.* (2004) analyse the hydro-mechanical coupled problem of the landslide of La Frasse. The influence of water table level, groundwater pressure, artificial drainage and constitutive laws (Hujieux-type and Mohr-Coulomb-type) have been analysed. After calculation, a good agreement was found between the simulations results and the in-situ tests when using Hujieux-type model. Mohr-Coulomb-type model under-estimated the displacements compared to reality. A fully coupled hydro-mechanical simulation of the Super-Sauze mud-slide was conducted by Malet (2003). The soil is described as an elasto-visco-plastic Hujieux-type material. The model is successful to predict a series of local failures during the increasing of pore water pressure as same as the observation. In the LESSLOSS project (BRGM 2007), BRGM contributes a 3D dynamic simulation of Corniglio-Lama landslide under an earthquake with a moment magnitude of 5.44. They developed a parallelised version of *GefDyn* to realise a dynamic analysis in a 3D large-scale simulation in order to reduce the time and to avoid the excess of computer's capacity.

This program is in continuous development at Ecole Centrale de Paris (LMSS-MAT). It has no commercial interface to handle and there is only a calculation-processor unlike *PLAXIS* which contains the pre- and post-processor. In this study, *GiD* was chosen as the pre- and post-processor to create the geometry, the mesh and also to view the results from *GefDyn*.

3 Geo-mechanical model

Landslides are observed in a variety of soils, but their dynamic analysis necessitates an adequate, non-linear model (Zienkiewicz *et al.* 1985). The choice of a constitutive model for the geomaterials found in landslides is complex. In landslide analysis, the Mohr-Coulomb model is still used, at least as a reference (Fifer Bizjak and Zupančič 2009). It was also used for dynamic analysis of soil behaviour, although it has obvious limitations when solicited in a stress loading path. For this reason, models that are able to represent the behaviour of geomaterials at the lab scale, during dynamic triaxial tests, as well as in real conditions, are preferred. The goal of this study being to establish a way to evaluate a generic case study, a model able to simulate the constitutive dynamic behaviour of a variety of soils is needed. The Hujeux model (Hujeux 1985) was specifically developed for a good representation of both sand and clays, which differ vastly by the shape of their respective yield surface in the p '- q plane. Its yield surface can be chosen from a Mohr-Coulomb type to a Cam-Clay type, and more importantly it uses the bounding surface theory to represent plastic strains created under the yield surface. These strains are necessary for a pertinent simulation of geomaterials cyclic behaviour. In this section, important features such as both monotonic and cyclic soil behaviours, hydro-mechanical coupling and boundary conditions are addressed.

3.1 Hujeux-ECP 1985 model

Soil has a non-linear dynamic behaviour even for small strain level, which is observed in experimental results (Rascal 2009). As a consequence, a realistic soil constitutive model should take this aspect into account by considering fundamental non-linearities of soil behaviour. Hujeux (1985) introduced an elasto-plastic constitutive law to describe the stress-strain relationship of soils under a wide range of levels of cyclic loading. This constitutive model uses four plastic mechanisms to describe the plastic behaviour (Aubry *et al.* 1982). Later improvements to this model were introduced by Mellal (1997), in the representation of soil behaviour under both monotone and cyclic solicitations. The model is written in terms of Terzaghi effective stress in the case of saturated soil. It uses incremental plasticity, critical state concept and Coulomb type yield criterion. The model takes into account contractive and dilative behaviour, the influence of effective pressure and kinematic hardening. The multi-mechanisms include three plane-strain deviatoric mechanisms ($k=1,2,3$), each in an orthogonal plan (\vec{e}_i^k, \vec{e}_j^k) and one purely isotropic ($k=4$). In which $i=1+mod(k,3)$ and $j=1+mod(k+1,2)$ with $mod(a,b)$ representing the residue of the division of a by b .

3.1.1 Notations

Several notations are defined here before introducing the Hujeux model.

Assuming in this chapter σ and ε as the tensor of the effective stress and the tensor of strains, we note in the space $(\vec{e}_i, \vec{e}_j, \vec{e}_k)$ that:

- $p = \frac{1}{3}(\sigma_{ii} + \sigma_{jj} + \sigma_{kk})$, the mean effective stress
- $\varepsilon_v = \varepsilon_{ii} + \varepsilon_{jj} + \varepsilon_{kk}$, the volumetric strain

- $S_{ij} = \sigma_{ij} - p\delta_{ij}$, the deviatoric stress tensor, δ_{ij} is Kronecker's delta ($\delta_{ij} = 1$, if $i = j$ and $\delta_{ij} = 0$, if $i \neq j$)
- $e_{ij} = \varepsilon_{ij} - \frac{\varepsilon_v}{3}\delta_{ij}$, the deviatoric strain tensor
- $q = \left(\frac{3}{2}S_{ij}S_{ji}\right)^{1/2}$, the deviatoric stress
- $\varepsilon = \varepsilon^e + \varepsilon^p$, the total strain is decomposed by the elastic strain ε^e and the plastic strain ε^p

Or equivalently in the two dimensional plane – in one mechanism k , the p , q and ε_v are written in the following forms:

- $p_k = \frac{1}{2}(\sigma_{ii} + \sigma_{jj})$, the centre of Mohr circle in the plane of deviatoric mechanism k
- $q_k = \sqrt{\frac{1}{4}(\sigma_{ii} - \sigma_{jj})^2 + \sigma_{ij}^2}$, the radius of Mohr circle in the plane of deviatoric mechanism k . Here we can consider that q_k is an Euclidean norm of the deviatoric stress vector $s_k = \left(\frac{\sigma_{ii} - \sigma_{jj}}{2}, \sigma_{ij}\right)$ and $q_k = \|s_k\|$, this notation will be used in the section 3.1.5.
- $(\varepsilon_v)_k = \varepsilon_{ii} + \varepsilon_{jj}$, the plane deformation in the plane of deviatoric mechanism k

3.1.2 Elasticity

In this model, the elastic component is an isotropic non-linear elastic behaviour with the bulk module (K_{max}) and shear module (G_{max}). These two modulus are functions of the mean compressive stress (p) as shown in [1]

$$K = K_{ref} \left(\frac{p}{p_{ref}}\right)^{n_e}; G = G_{ref} \left(\frac{p}{p_{ref}}\right)^{n_e} \quad [1]$$

Where K_{ref} and G_{ref} are respectively the bulk and shear modulus at the mean reference effective pressure p_{ref} , or we call them initial modulus at the first sollicitation. The exponent n_e controls the degree of non-linearity. In the case that n_e equals to zero, the soil behaves a linear elasticity.

3.1.3 Deviatoric mechanisms

3.1.3.1 Yield function and hardening laws for monotonic loading

This constitutive law uses a yield function presenting a strong generalization of the Coulomb friction law. The deviatoric mechanism k in the plan of $(\vec{e}_i^k, \vec{e}_j^k)$ for a monotonic path (index m) is governed by the following yield function:

$$f_k^m = q_k - \sin \phi p_k F_k r_k^m \quad [2]$$

Where several parameters are defined as,

- ϕ , the soil friction angle at the perfect plasticity
- $F_k = 1 - b \ln \frac{p_k}{p_c}$, this generalization function depends on the actual stress state and takes into the volumetric hardening and softening using parameter p_c . If $b=0$, the yield function is back to standard Coulomb friction.
- p_c , the critical pressure (also called pre-consolidation pressure) that is related to the volumetric plastic strain ε_v^p . The relationship is defined as $p_c = p_{c0} \exp(\beta \varepsilon_v^p)$, β is the plastic compressibility of the material in the isotropic plane ($\ln p', \varepsilon_v^p$), and p_{c0} is the initial critical pressure (or called initial pre-consolidation pressure). The critical pressure is unique for the four mechanisms.
- b , the numeric parameter varying from 0 to 1 controls the shape of the yield function, ($b = 0$ for Mohr-Coulomb yield criterion and $b = 1$ for Cam-clay yield criterion) as shown in Figure 5.
- r_k^m , is called the degree or the radius of mobilized friction. The value varies from an elastic radius to 1 in the perfect plasticity. This parameter creates a bounding surface linked with the yield surface, as shown in Figure 5.

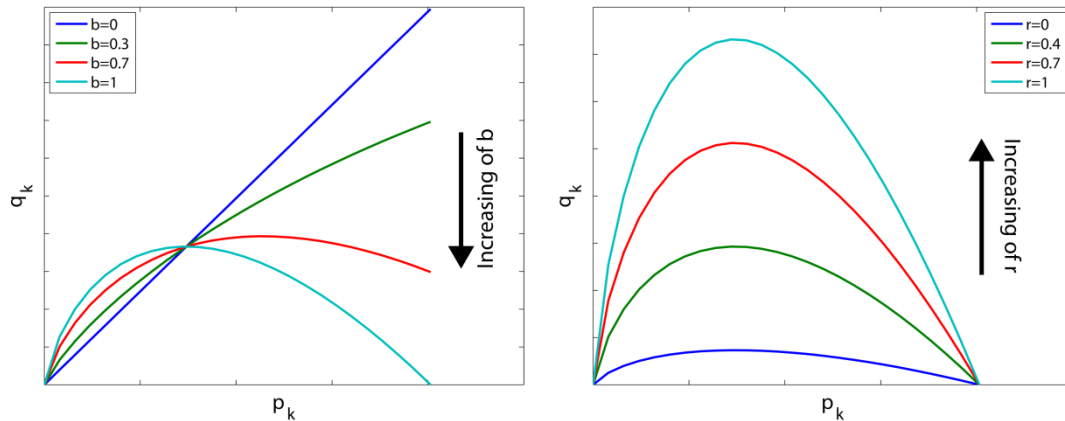


Figure 5 Influence of the numerical parameter (b) and the degree of mobilized friction (r) on the yield surface shape.

In order to take into account the iterative calculation and distinguish precedent step $i-1$, the actual step i and the next step $i+1$, the component exponent i is added to the variable r_k as r_k^i . r_k^i is an important parameter that is related to the plastic deviatoric strain $\varepsilon_{d,k}^p$ and an internal variable a as shown in the following relationship

$$r_k^i = r_k^{el} + \frac{\int d\varepsilon_{d,k}^p dt}{a + \int d\varepsilon_{d,k}^p dt} \quad [3]$$

Where, a varies between two variables a_1 and a_2 by the relation of $a = a_1 + (a_2 - a_1)\zeta(r_k^{i-1})$, or in another notation like $a = a_c + (a_m - a_c)\alpha(r_k^{i-1})$. The first formulation is used in this document.

$$\zeta(r_k^i) = \begin{cases} 0 & \text{if } r_k^{i-1} \leq r_k^{hys} \text{ pseudo-elastic behavior} \\ \left(\frac{r_k^{i-1} - r_k^{hys}}{r_k^{mbl} - r_k^{hys}} \right)^m & \text{if } r_k^{mbl} \leq r_k^{i-1} \leq r_k^{hys} \text{ hysteretic behavior} \\ 1 & \text{if } r_k^{i-1} \geq r_k^{mbl} \text{ plastic mobilization} \end{cases} \quad [4]$$

r_k^{el} , r_k^{hys} and r_k^{mbl} are the limit for the elastic domain, the hysteretic domain and the occurrence of plastic mobilization, respectively.

The flow rule in the Hujeux model can be an associated or non-associated flow rule for each mechanism in its relative plane depending on the dilatancy coefficient α_ψ . And it is based on a Roscoe-type dilatancy law for the volumetric plastic strain:

$$\dot{\epsilon}_{v,k}^P = \dot{\lambda}_k^P \left[-\alpha_\psi \zeta(r_k^{i-1}) \left(\sin \psi + \frac{q_k}{p_k} \right) \right] \quad [5]$$

In which, α_ψ and ψ are the dilatancy coefficient and dilatancy angle, respectively. If α_ψ is not equal to 1, the flow rule will be a non-associated one. As shown in the Figure 6, the dilatancy angle ψ defines the limit between the dilating ($\dot{\epsilon}_{v,k}^P > 0$) and contracting ($\dot{\epsilon}_{v,k}^P < 0$) behavior of soil material.

In the plan of (p, q) , the line of $q = p \sin \psi$ is the characteristic line. $\dot{\lambda}_k^P$ in this equation is the plastic multiplier of each mechanism k , which can be determined by the consistency relationship.

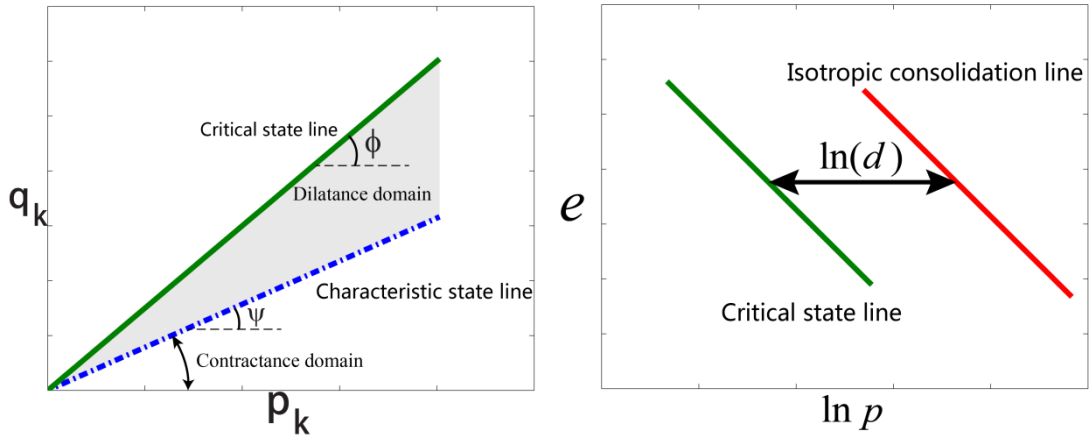


Figure 6: (left) Critical state line and characteristic state line. (right) Definition of numerical parameter d

3.1.3.2 Yield function and hardening laws for cyclic loading

Once a stress reversal occurs, the primary monotone yield surface will be abandoned. The cyclic yield surface based on the primary monotone yield function will be switched on, written in the following form:

$$f_k^{cyc} = q_k^{cyc} - \sin \phi p_k F_k r_k^{cyc} \quad [6]$$

Where q_k^{cyc} is the cyclic stress deviator which is defined in the section 3.1.5. The cyclic radius r_k^{cyc} during the cyclic loading is written in the same way as monotonic radius r_k^m :

$$r_k^{cyc} = r_k^{el} + \frac{\int d\varepsilon_{d,k}^p dt}{a + \int d\varepsilon_{d,k}^p dt} \quad [7]$$

Whenever a reversal occurs, the variable r_k^{cyc} and c_k are discontinuously updated (Modaressi *et al.* 2008).

3.1.4 Isotropic mechanisms

The multi-mechanism model not only takes into account the deviatoric behaviour, but also the isotropic behaviour in order to complete the constitutive law. The isotropic yield function defines the last mechanism $k = 4$ (isotropic) as shown in the Eq.[8]

$$f_{iso(k=4)} = p - p_c r_{k=4} d \quad [8]$$

Where p is the current state mean e effective pressure and d is the distance between the isotropic consolidation line and the critical state line in the plane of $(\ln p, e)$, which is shown in the Figure 6.

The radius $r_{k=4}$ and model parameter c control the degree of volumetric mobilization of soil and defined as:

$$r_{k=4} = r_{k=4}^{el} + \frac{\int d\varepsilon_{v,k=4}^p dt}{c P_c / p_{ref} + \int d\varepsilon_{v,k=4}^p dt} \quad [9]$$

The parameter c takes the value equalled to c_m or c_{cyc} for monotonic or cyclic loading respectively.

All the four mechanisms are coupled through the total volumetric plastic strain ε_v^p given by :

$$d\varepsilon_v^p = d\varepsilon_{v,k=1}^p + d\varepsilon_{v,k=2}^p + d\varepsilon_{v,k=3}^p + d\varepsilon_{v,iso(k=4)}^p \quad [10]$$

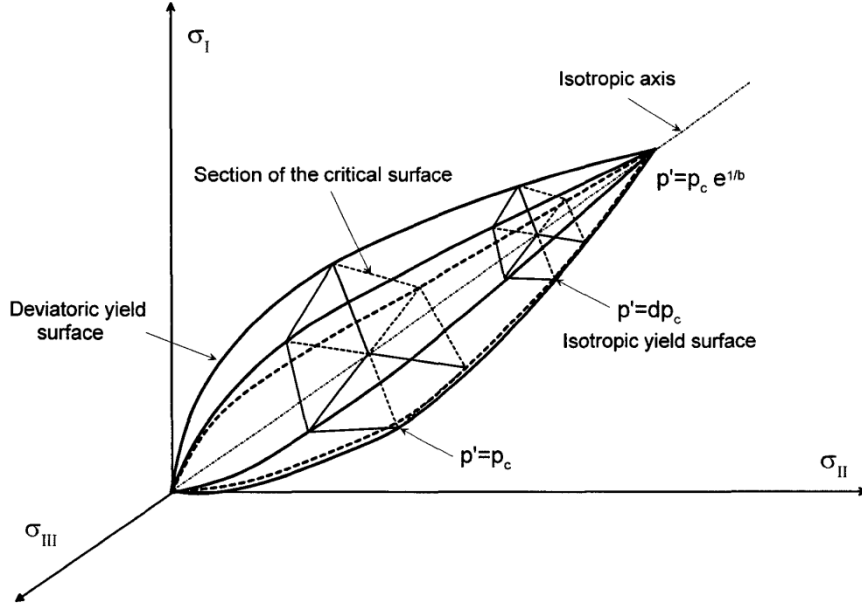


Figure 7: Yield surface in the principal stress plane (Cekerevac 2003)

3.1.5 Interpretation of ECP-Hujeux model

In this section, the role of yield functions for one deviatoric mechanism k in a normalized stress plane is explained schematically. First, the definition of this normalized stress for monotonic behaviour will be described. The definition for cyclic loading part will be followed. A schema at the end of this section will be discussed in detail in order to understand how the model predicts the soil behaviour.

The deviatoric stress vector s_k defined in the section 3.1.1 and the monotonic yield surface Eq.[2] defined in the section 3.1.3.1 can be normalized by $\sin \phi p_k F_k$ and then they become,

$$\tilde{f}_k^m = \frac{q_k}{\sin \phi p_k F_k} - r_k^m = \frac{\|s_k\|}{\sin \phi p_k F_k} - r_k^m = \|\tilde{s}_k\| - r_k^m \leq 0 \quad [11]$$

$$\tilde{s}_k = \frac{s_k}{\sin \phi p_k F_k} = \left(\frac{\sigma_{ii} - \sigma_{jj}}{2} \frac{1}{\sin \phi p_k F_k}, \frac{\sigma_{ij}}{\sin \phi p_k F_k} \right) = (\tilde{s}_{k1}, \tilde{s}_{k2}) \quad [12]$$

Combining Eq.[11] and Eq.[12], the normalized yield surface then becomes a circle in the plane of normalized deviatoric stress vectors $(\tilde{s}_{k1}, \tilde{s}_{k2})$ with a radius equalled to r_k^m .

$$\|\tilde{s}_k\| - r_k^m \leq 0 \Leftrightarrow (\tilde{s}_{k1})^2 + (\tilde{s}_{k2})^2 \leq (r_k^m)^2 \quad [13]$$

The Hujeux model has an important feature describing the kinematic hardening. Figure 8 is a schematic illustration of the feature of Hujeux model. When the monotonic stress path leaves the elastic domain, the inner yield surface will be activated and start to increase its size remaining unchanged in the shape, with radius r_k^m growing. Cyclic yield surface will become active instead of the primary monotonic yield function when a reversal occurs – or a change in the loading direction.

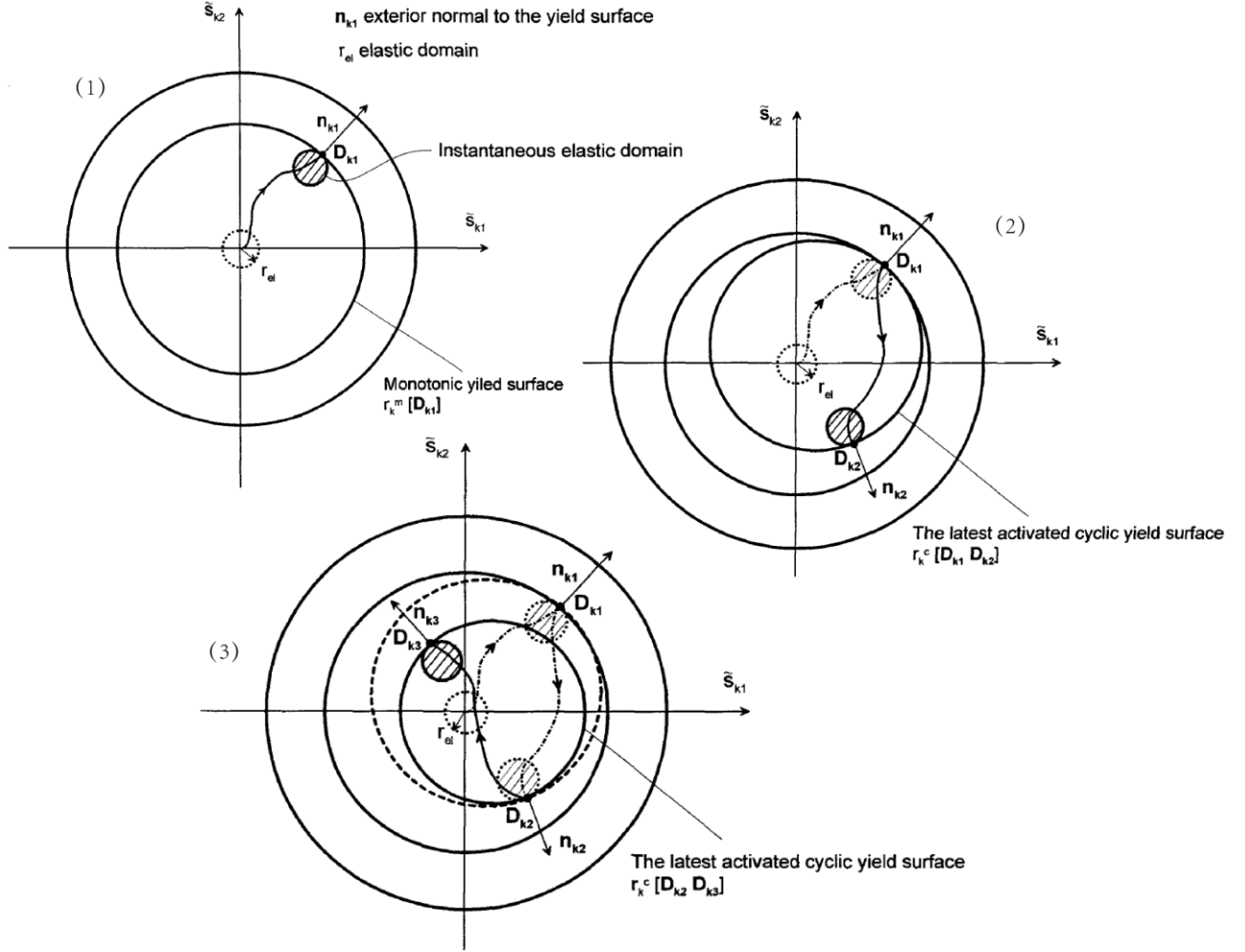


Figure 8: Evolution of yield surface in the monotonic condition (1) and cyclic conditions (2) and (3). (Cekerevac 2003)

During the loading, the soil remains in the “instantaneous elastic domain” at the point $D_{k,i}$. This domain is defined by the normal vector $n_{k,i}$, which is in the radial direction of both the originating yield surface and the instantaneous elastic domain. After each change in the direction of loading, the elastic domain will be re-initialized by the radius r_k^{el} and the couple of $(D_{k,i}, n_{k,i})$. Here the index i represents the i th times of changing loading direction in the mechanism k .

The yield function for cyclic loading mentioned in the section 3.1.3.2 has a deviatoric stress q_k^{cyc} , which is defined as follows:

$$q_k^{cyc} = \|s_k^c\| = \left\| s_k - (D_{i,k} - n_{i,k} r_k^{cyc}) \sin \phi p_k F_k r_k^{cyc} \right\| \quad [14]$$

Then the cyclic yield function Eq.[6] can be also normalized as the same way as the monotonic one:

$$\tilde{f}_k^{cyc} = \frac{q_k^{cyc}}{\sin \phi p_k F_k} - r_k^{cyc} = \left\| \tilde{s}_k - (D_{i,k} - n_{i,k} r_k^{cyc}) \right\| - r_k^{cyc} \leq 0 \quad [15]$$

More details and full descriptions about this model can be found in (Aubry *et al.* 1982; Hujeux 1985).

3.2 Governing equations for poroelastic media

The motion of pore fluid has an influence on the deformations of the solid skeleton of the soil or rock. The choice for formulation of this phenomenon is therefore important to be established for this study. Several choices are available in the literatures. In general, the soil is considered as a saturated material of two-phase composition in a dynamic analysis. Unsaturated soils will not be considered. In this section, a generalized Biot formulation is described. Then for different requirements of study cases, simplified formulations will be proposed. The three main equations governing the interaction of these two phases, the motion equation, mass equation and the Darcy equation have been shown in Eq.[16], Eq. [18] and Eq.[19] :

The momentum conservation for the soil-fluid mixture is given by:

$$\mathbf{div} \boldsymbol{\sigma} + \rho \underline{\underline{g}} = \rho \ddot{\underline{\underline{u}}}_s + \rho_f \ddot{\underline{\underline{u}}}_{rf} \quad [16]$$

In terms of effective stress, it becomes:

$$\mathbf{div} \boldsymbol{\sigma}' - \mathbf{grad} p + \rho \underline{\underline{g}} = \rho \ddot{\underline{\underline{u}}}_s + \rho_f \ddot{\underline{\underline{u}}}_{rf} \quad [17]$$

Where

- $\underline{\underline{g}}$ is the gravity acceleration vector,
- p , the pore water pressure,
- $\boldsymbol{\sigma}$, $\boldsymbol{\sigma}'$ the total Cauchy stress, effective stress in the combined solid and fluid mix at any instant,
- ρ , the density of assembly $\rho = (1-n)\rho_s + n\rho_f$,
- n , the porosity of the porous medium,
- ρ_f , ρ_s , the density of fluid phase and the density of solid phase,
- $\underline{\underline{u}}_s$, the displacement of solid phase,
- $\underline{\underline{u}}_{rf}$, the relative displacement to the solid phase $\underline{\underline{u}}_{rf} = n(\underline{\underline{u}}_f - \underline{\underline{u}}_s)$,
- The divergence operator is defined as $\{\mathbf{div}(\boldsymbol{\sigma}_{ij})\}_i = \sum_j \partial_j \boldsymbol{\sigma}_{ij}$,
- The gradient operator is defined as $\{\mathbf{grad}(p)\}_i = \partial_i p$.

The mass conservation for a saturated two-phase medium is written in the Eq.[18]

$$\mathbf{div} \dot{\underline{\underline{u}}}_{rf} + \mathbf{div} \dot{\underline{\underline{u}}}_s = -\frac{\partial_t p}{Q} \quad [18]$$

Where the compressibility variable Q is defined as $\frac{1}{Q} = \frac{n}{K_f} + \frac{1-n}{K_s}$ in which K_s and K_f are respectively the compressibility of solid and fluid phase.

A generalized Darcy law governs the movement of one phase with respect to the other:

$$\dot{\underline{\underline{u}}}_{rf} = \mathbf{K} \left[-\mathbf{grad} p + \rho_f (\underline{\underline{g}} - \ddot{\underline{\underline{u}}}_s - \ddot{\underline{\underline{u}}}_{rf} / n) \right] \quad [19]$$

where \mathbf{K} is a tensor of permeability which is defined as $\mathbf{K} = \mathbf{k}_i / \rho_f \underline{g}$ in three principal directions (x, y, z) . Usually, the permeability in the soil is considered isotropic ($k_x = k_y = k_z$).

Eq.[19] then can be putted into Eq.[18], we obtained:

$$\text{div } \underline{\dot{u}}_s + \text{div} \left\{ \mathbf{K} \left[-\text{grad } p + \rho_f (\underline{g} - \underline{\ddot{u}}_s - \underline{\ddot{u}}_{rf} / n) \right] \right\} = -\partial_t p / Q \quad [20]$$

The flow of pore-fluid for low permeability values is governed by seepage rather than inertial effects (Benzenati and Modaressi 1994). In addition, the acceleration of solid skeleton is much higher than that of fluid phase which therefore can be neglected in the Darcy relationship (i.g. $\underline{\ddot{u}}_{rf}$ is eliminated in Eq.[19]). This formulation called first simplified model 'FSM' or u_s - u_{rf} - p formulation:

$$\text{FSM} \begin{cases} \text{div } \underline{\sigma}' - \text{grad } p + \rho \underline{g} = \rho \underline{\ddot{u}}_s + \rho_f \underline{\ddot{u}}_{rf} \\ \text{div } \underline{\dot{u}}_s + \text{div} \left\{ \mathbf{K} \left[-\text{grad } p + \rho_f (\underline{g} - \underline{\ddot{u}}_s) \right] \right\} = -\partial_t p / Q \end{cases} \quad [21]$$

This formulation is interesting for the loading with a high frequency, for example a frequency above 30Hz (Zienkiewicz and Shiomi 1984; Modaressi 2003; De Martin *et al.* 2007). In the earthquake engineering, the frequency for the loading is not as high as that for the first simplified model. A further assumption can be made in the case of lower frequencies. The relative fluid acceleration can also be neglected in momentum conservation equation (i.g. $\underline{\ddot{u}}_{rf}$ is eliminated in Eq.[16] and Eq.[17]).

In such case, the unknown variables are just the solid displacement and pore water pressure. This model is more often called u - p formulation:

$$\text{SSM} \begin{cases} \text{div } \underline{\sigma}' - \text{grad } p + \rho \underline{g} = \rho \underline{\ddot{u}}_s \\ \text{div } \underline{\dot{u}}_s + \text{div} \left\{ \mathbf{K} \left[-\text{grad } p + \rho_f (\underline{g} - \underline{\ddot{u}}_s) \right] \right\} = -\partial_t p / Q \end{cases} \quad [22]$$

A further assumption can be made in some cases. The acceleration of solid in the Darcy law can be neglected in the case of relatively rigid layers, returning the second equation back to the basic Darcy law. As a result, the third simplified formulation 'TSM' (u -Biot formulation) can be obtained:

$$\text{TSM} \begin{cases} \text{div } \underline{\sigma}' - \text{grad } p + \rho \underline{g} = \rho \underline{\ddot{u}}_s \\ \text{div } \underline{\dot{u}}_s + \text{div} \left\{ \mathbf{K} \left[-\text{grad } p + \rho_f \underline{g} \right] \right\} = -\partial_t p / Q \end{cases} \quad [23]$$

3.2.1 Application domains

In the previous section, the main governing equations are described and a set of assumptions presented. However, the application domains are only talked about ambiguously in terms of the characteristics of the loading and of the site. In this section, their own domains of application are addressed quantitatively for the three simplified formulations. In fact, the coupling problem depends on several aspects such as frequency of solicitation, soil depth and characteristics of soil. For example, if the loading with a low frequency reacts on a deep soil, the influence of fluid cannot be neglected in terms of acceleration. Zienkiewicz and Shiomi (1984) and Modaressi (2003) introduced in their works two parameters to define whether or not the coupling problem needs to be taken into account in the study for one-dimensional soil column:

$$\Pi_1 = K\rho c_p^2 / \omega L^2 ; \Pi_2 = \omega L / c_p$$

in which, c_p is the p-wave velocity in the soil, L the characteristic depth and ω is the angular frequency of applied loading.

With these two dimensionless quantities, Figure 9 shows the domain of application:

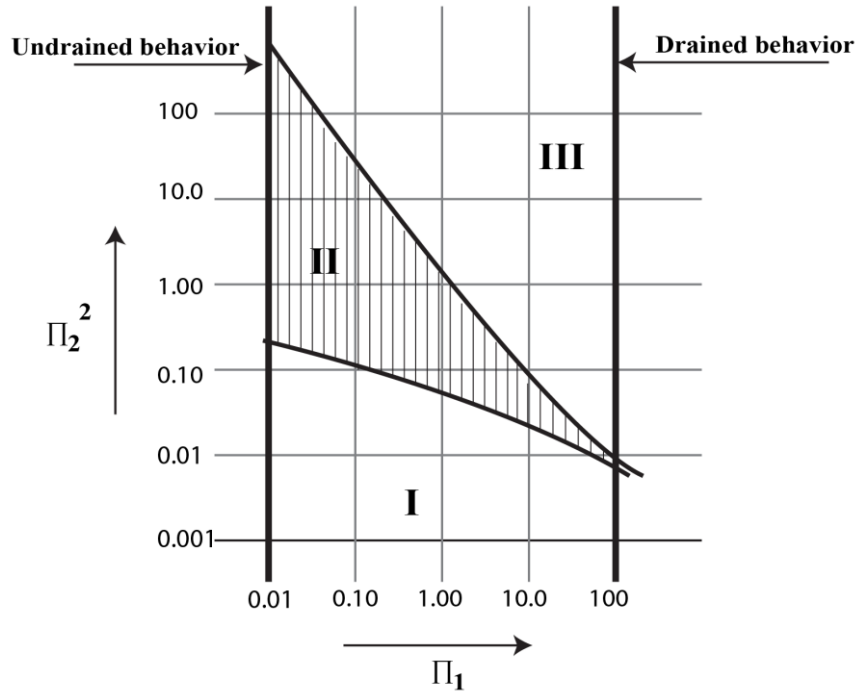


Figure 9: Domain of application for three models (from Zienkiewicz and Shiomi (1984))

Zone I : $\ddot{\mathbf{u}}_{rf}$ can be neglected, and $\ddot{\mathbf{u}}_s$ can be neglected in Darcy law - ‘TSM’

Zone II : $\ddot{\mathbf{u}}_{rf}$ can be neglected - ‘SSM’

Zone III : $\ddot{\mathbf{u}}_{rf}$ can be neglected in momentum conservation equation - ‘FSM’

To calculate the two parameters, the main frequency is chosen as 5Hz for an earthquake input. The p-wave in soil stratum of *Les Peillettes* is estimated in the range of 500 m/s. The permeability of soil is assumed as 10^{-5} m/s. An average depth of 40 m is chosen for the calculation. The case for *Les Peillettes* is in the Zone II under earthquake’s loading. A $u-p$ formulation is then necessary to be implemented in the modelling of *Les Peillettes*.

3.3 Paraxial element

In reality, wave will dissipate energy during propagating in the soil. Dynamically studied sites are always modelled as a finite geometry with several boundary conditions in order to represent semi-infinite soil. In addition, lateral boundary should be “far away” so as not to influence the deformation behaviour or stress wave propagation. However locating the boundaries far away requires a huge geometry, more elements and leads to a more costly simulation. Adapted boundary conditions are necessary to avoid reflection and perturbations on the model boundaries. In earthquake engineering, the absorbent boundary is still a technical challenge due to its difficulty in the mathematical formulation to simulate the real local boundary in the soil.

Figure 10 is a schematic illustration of the problem. The seismic waves are generated by earthquake faults in an infinite elastic medium $\Omega_{s'}$ (usually it is the infinite bedrock). The domain of interest consists of an interior elastic domain Ω_s (a thin layer of bedrock below the soil) and the interface Σ along the outside of Ω_s and inelastic soil domain Ω_{in} . To simulate the infinite domain $\Omega_{s'}$, is often time-consuming in terms of calculation. The medium $\Omega_{s'}$ can be simulated as the radiation condition at the base of interesting domain (at the interface Σ) by absorbent elements which are called paraxial elements. These elements are implemented into *GeFDyn*.

Paraxial element allows reflected waves to be evacuated from the study domain and avoid any artificial reflection on the interface. To obtain the local impedance of soil, the development is performed on the elasto-dynamic equations in Fourier domain. The detailed mathematical formulation can be referred to (Benzenati and Modaressi 1994; Modaressi 2003). In this section, the variational formulation will be described in one dimension in order to understand how paraxial element plays a role in the finite element method.

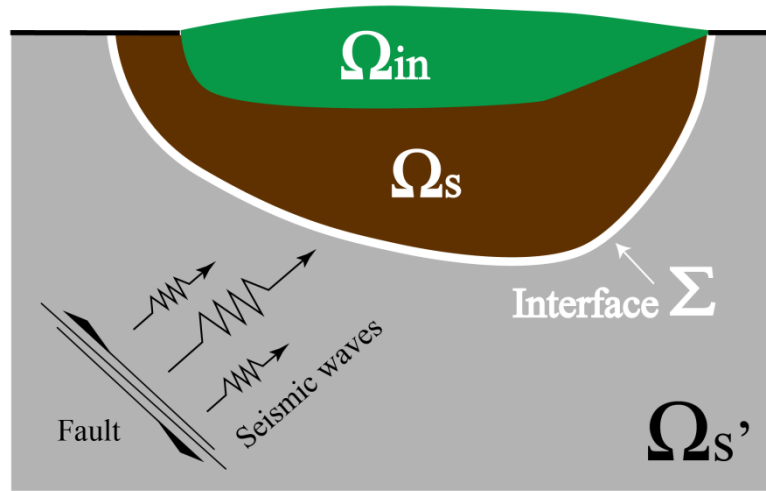


Figure 10: Schematic illustration of soil medium.

At the interface Σ between the two mediums Ω_s and $\Omega_{s'}$, the displacement and the stress vector should be continued:

$$\begin{cases} \underline{u}_s = \underline{u}_{s'} \\ \underline{\tau}_s + \underline{\tau}_{s'}(\underline{u}_{s'}) = 0 \end{cases} \quad [24]$$

$\underline{u}_{s'}$ is decomposed into two components, an incident wave field \underline{u}_i and a diffraction field \underline{u}_d :

$$\underline{u}_{s'} = \underline{u}_i + \underline{u}_d \quad [25]$$

In the medium $\Omega_{s'}$, the stress due to the diffraction is approached by the zero-order paraxial element for the stress vector at the interface Σ is:

$$\underline{\tau}_{s'}(\partial_t \underline{u}_{s'}) = \mathbf{A}_0(\partial_t \underline{u}_{s'}) = \rho \mathbf{C} \partial_t \underline{u}_{s'} \quad [26]$$

where \mathbf{A}_0 is the paraxial operator that models approximately the stress vector in the elastic medium where the wave propagates in one direction. \mathbf{C} is the wave velocity tensor which is defined as

$$\mathbf{C} = \begin{bmatrix} C_s & 0 & 0 \\ 0 & C_s & 0 \\ 0 & 0 & C_p \end{bmatrix} \text{ where } C_s \text{ and } C_p \text{ are the shear wave velocity and pressure wave velocity,}$$

respectively.

Considering that the neighbourhood of interface Σ is linear elastic. After the zero-order approximation with Eq.[24] and Eq.[25], we can derive that:

$$\begin{aligned} \underline{\tau}_s &= -\underline{\tau}_{s'}(\underline{u}_{s'}) = -\underline{\tau}_{s'}(\underline{u}_{i'}) - \underline{\tau}_{s'}(\underline{u}_{d'}) \\ &\square -\underline{\tau}_{s'}(\underline{u}_{i'}) - \mathbf{A}_0(\partial_t \underline{u}_{d'}) \\ &\square -\underline{\tau}_{s'}(\underline{u}_{i'}) - \mathbf{A}_0(\partial_t \underline{u}_{s'}) + \mathbf{A}_0(\partial_t \underline{u}_{i'}) \end{aligned} \quad [27]$$

This equation represents the evolution of stress at the interface Σ . One can notice that the wave velocity and the field $\underline{\tau}_{s'}(\underline{u}_{i'})$ are required. The variational formulation in the virtual work principles with a virtual work w is then written as follows and can be implemented in FEM:

$$\begin{aligned} \int_{\Omega_s} \rho \partial_{tt} \underline{u}_{s'} \cdot \underline{w} d\Omega + \int_{\Omega_s} \underline{\sigma}_{s'} : \underline{\varepsilon}(\underline{w}) d\Omega + \int_{\Sigma} \mathbf{A}_0(\partial_t \underline{u}_{s'}) \cdot \underline{w} d\Sigma = \\ \int_{\Omega_s} \rho \underline{g} \cdot \underline{w} d\Omega + \int_{\Sigma} (-\tau_{s'}(\underline{u}_{i'}) + \mathbf{A}_0(\partial_t \underline{u}_{i'})) \cdot \underline{w} d\Sigma \end{aligned} \quad [28]$$

4 Dynamic analysis for *Les Peillettes*

4.1 Elementary test

In order to evaluate the soil behaviour under both monotonic and cyclic loading, elementary test were carried out. The material parameters are listed in Table 2. Since only geological information is available, the soil material parameters are estimated by considering the local conditions of geology and combining the information from literature on dynamic simulation of geo-materials (López-Caballero 2003).

	Soil cover #1	Slide surface	Soil cover #2	Grand-Tsâble	Rock
Elasticity					
K_{ref} (M Pa)	444	275	525	780	1538
G_{ref} (M Pa)	222	128	376	550	3333
n_e	0.3	0.3	0.3	0.3	1.0
p_{ref} (M Pa)	1.0	1.0	1.0	1.0	1.0
Critical State and Plasticity					
ϕ'_{pp} (°)	33	30	35	35	
β	43	30	43	35	
d	1.8	3.5	3.5	3.5	
b	0.2	0.12	0.2	0.2	
p_{co} (M Pa)	1.8	0.53	1.8	1.8	
Flow Rule and Isotropic Hardening					
ψ (°)	33	30	35	35	
α_{ψ}	1.0	1.0	1.0	1.0	
a_1	1.0E-4	1.0E-4	1.0E-4	1.0E-4	
a_2	4.0E-4	4.0E-4	4.0E-4	4.0E-4	
c_1	0.06	0.06	0.06	0.06	
c_2	0.03	0.03	0.03	0.03	
m	1.0	1.0	1.0	1.0	
Threshold Domains					
r^{ela}	5.0E-3	1.0E-2	5.0E-3	5.0E-3	
r^{hys}	1.0E-2	5.0E-2	3.0E-2	1.0E-2	
r^{mob}	8.0E-2	8.0E-1	8.0E-2	8.0E-1	
r^{mob}_{iso}	1.0E-4	1.0E-4	1.0E-4	1.0E-4	

Table 2: Parameters of Hujeux ECP 4 Mechanisms for the landslide of *Les Peillettes*

Figure 11 represents numerical simulations of the elementary triaxial tests in the drained condition with Hujeux-ECP model. The initial confining pressures p_0 are defined according to the soil weight at various elevations. An axial strain of 0.2 is then applied to all samples. The results show the soil sample exhibits the normally consolidated behaviour with a plateau for the shear strength and the volume compression in general.

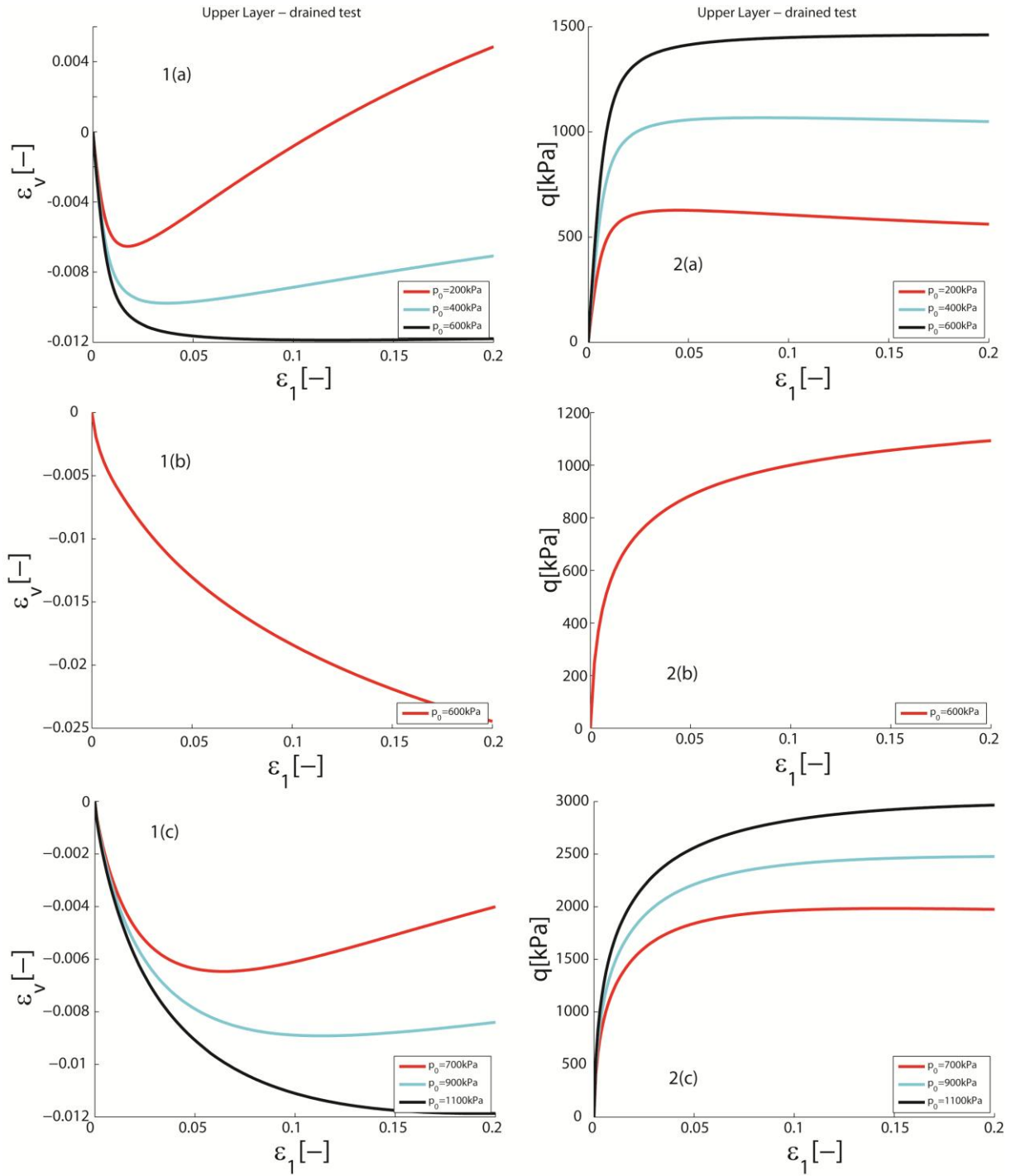


Figure 11: Triaxial compression tests in drained conditions. Figures with index 1 are in the plane of volumetric strain ε_v – axial strain ε_1 . Figures with index 2 are in the plane of deviatoric stress q - axial strain ε_1 . Index (a) represents soil cover #1, (b) represents slide surface and (c) represents soil cover #2.

However, in some cases such as at confining pressure $p_0 = 200kPa$ in soil cover #1 (Figure 11.a) and $p_0 = 700kPa$ in soil cover #2 in (Figure 11.c), samples exhibit dilatant behaviour. The drained tests were used to illustrate and verify the behaviour of assumed soil parameters.

Using these material parameters, simulations of undrained triaxial tests were carried out for the three layers of soil.

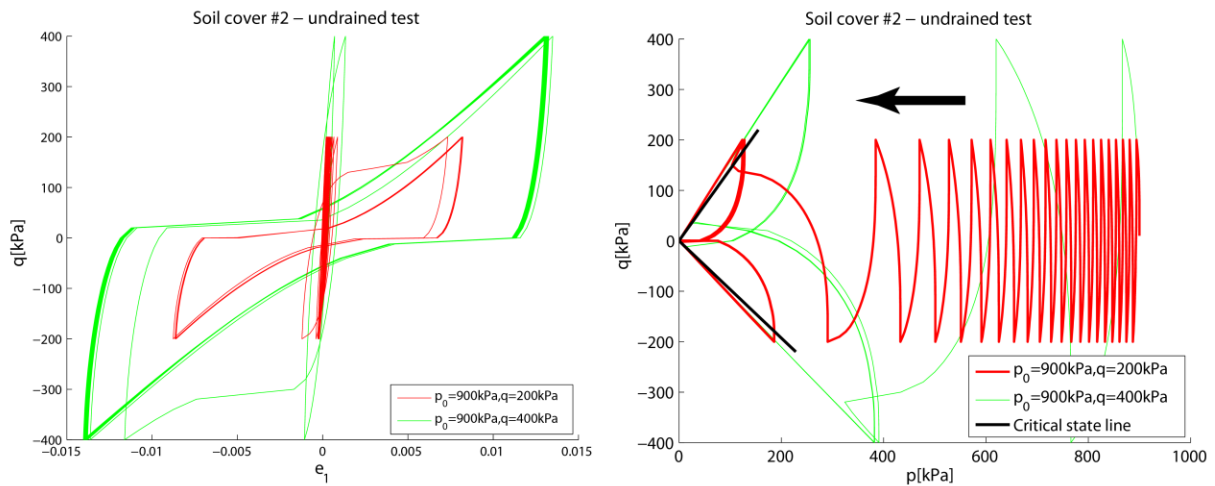


Figure 12: Cyclic triaxial compression tests of soil cover #2 in undrained conditions, (left) in the plane of $q - \varepsilon_1$; (right) in the plane of mean effective stress p' - deviatoric stress q .

Figure 12 represents the stress-strain response of the soil cover #2 in undrained cyclic stress-imposed triaxial tests. The test is carried out with one confining pressure (900kPa) and two levels of deviatoric stress (200kPa and 400 kPa). In the $q - \varepsilon_1$ plane, the cyclic mobilisation can be observed. In the $p' - q$ plane, 20 cycles are needed in the 200kPa-test to trigger soil failure. For the test with $q=400$ kPa failure occurs after just two cycles of loading. The decrease of effective mean stress is due to the increase of pore water pressure, which can be demonstrated by Figure 13. In this figure, the ratio between the pore water pressure and initial confining pressure is shown against to the number of cycles. In the case of $q=200$ kPa, excess pore pressure accumulates from the beginning of loading in a controlled manner. After 20 cycles, the ratio increases roughly to 1. Regarding the response of $q=400$ kPa, the ratio equals 1 after two cycles of loading, which corresponds to the observation of stress-strain responses.

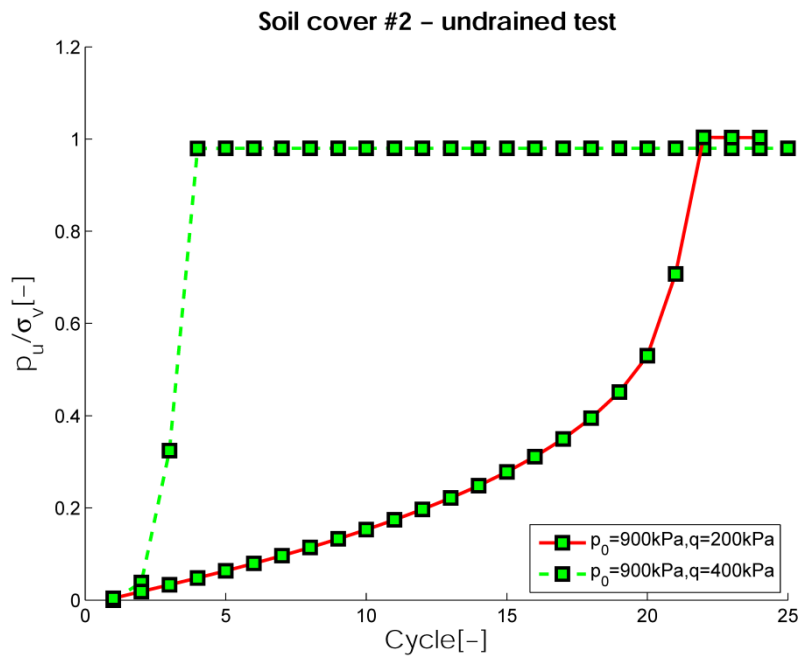


Figure 13: Ru ratio evolution of triaxial cyclic tests

4.2 Finite element model

The adopted finite element mesh is shown in Figure 14. The geometry is discretized with 5175 3-node triangle elements. The mesh is refined in the soil covers and slide surface. On the basis of the results from drilling borehole investigations, five different materials were considered with different mechanical characteristics (see the coloured zones in Figure 14). The top of landslide at right hand is fixed in horizontal displacement during the whole simulation.

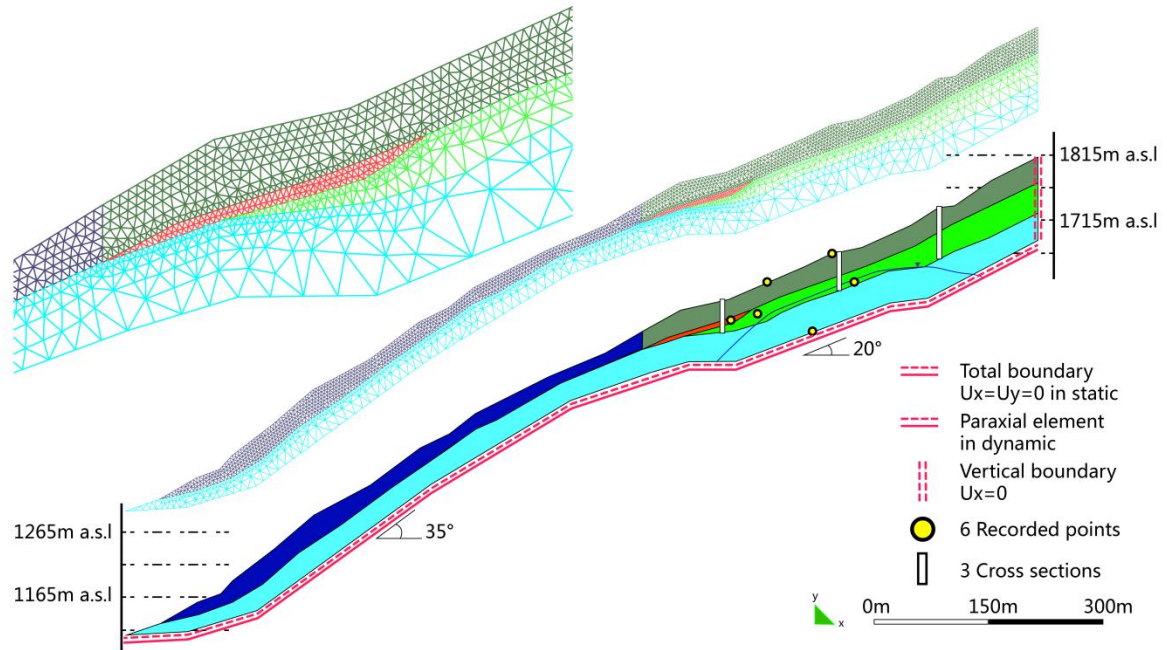


Figure 14: Finite element mesh and boundary conditions of the landslide *Les Peillettes*. Dark green: soil cover with 1740 elements; Dark blue: soil cover with 1579 elements; Red: slip plan with 231 elements; Light green: soil cover with 552 elements; Light blue: bedrock with 1073 elements.

Six points and three cross sections are chosen to save the node results during the whole simulation, such as acceleration, displacement and pore-water pressure. Stress and strain at real nodes are obtained by the interpolation from the integration points to real nodes. The pore-water pressure at surface of the soil is supposed to be zero.

In order to get the initial state, the nodes along the bottom of the landslide are fixed in both vertical and horizontal directions. The initial state of stress is generated only considering soil weight at rest. The initial hydraulic stress is hydrostatic pressure induced by ground water table. Above the water table, the soil is considered either as dry, or as saturated with infiltrating water where pressure is zero. This condition of infiltrating water is seen in cases of heavy rain or snow melting, though the zero pressure condition remains an assumption. Figure 15 shows the distribution of pore pressure in landslide body and also the effective vertical stress at steady state condition.

During dynamic stage, the nodes at the bottom are constrained in the horizontal and vertical direction in order to apply seismic input motions and activate the paraxial elements.

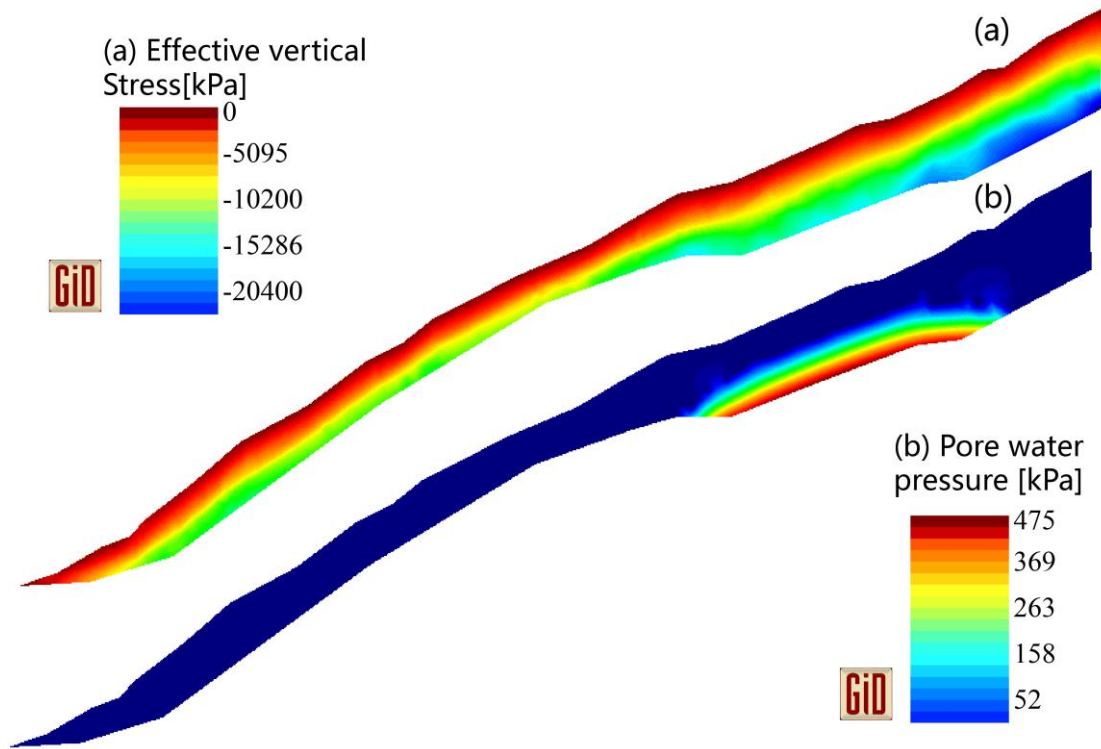


Figure 15: Initial condition: (a) distribution of effective vertical stress. (b) distribution of pore pressure.

The acceleration time history applied at the bedrock is shown in Figure 16, which has a moment magnitude of 5. This accelerogram is taken from the *GefDyn* library and adapted to *Les Peillettes* by the theory of deconvolution (Kramer 1996). The vertical motion is assumed as 0.01 times the whole horizontal acceleration input.

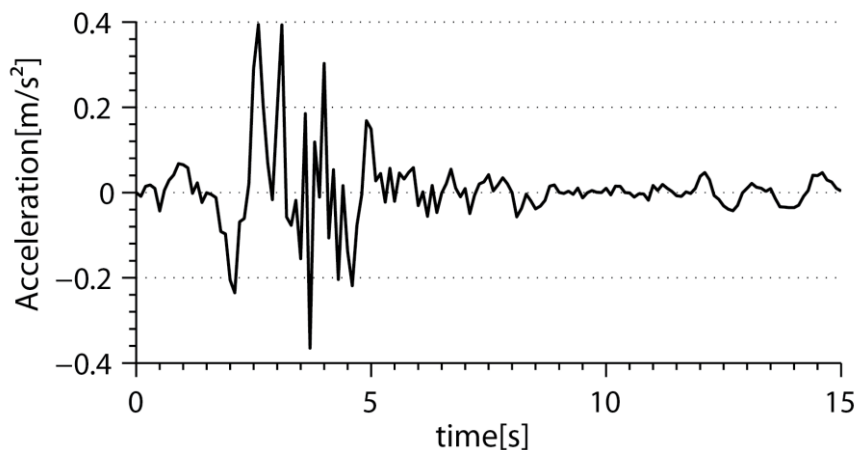


Figure 16: Input horizontal accelerogram

Various simulations allow comparisons among constitutive behaviours of soil, hydraulic conditions and exterior solicitations. Responses to the seismic loading are firstly studied using Mohr-Coulomb and Hujoux models. Considering climate variations in *Les Peillettes*, in spring the melting of snow results in a high infiltration in the soil, therefore the soil in the model is then considered as totally saturated during dynamic calculation. On the other hand, in summer the soil is not saturated at all. For this reason, a scenario of dry soil is also taken into consideration. Finally, the case of a stronger earthquake was considered: horizontal and vertical input accelerations were both doubled in amplitude as one scenario for the study.

4.3 Response to the earthquake

The responses of ground acceleration for the case of saturated soil covers using Hujoux-ECP model and Mohr-Coulomb model are shown in Figure 17. Very important differences are found, especially in the upper zones of the soil. As can be observed in the figure, the Mohr-Coulomb model predicts much less acceleration than the Hujoux-ECP model in the shallower areas. This difference results from the way that two constitutive laws take into account the progressive soil hardening in their formulations. This observation is also found by (Laloui *et al.* 2004). They state that the numerical results obtained by Hujoux ECP model are closer to the observed data than that obtained by Mohr-Coulomb model. The effects of a reactivated cyclic behaviour of the soil are obvious and justify the use of the more advanced model for this case study.

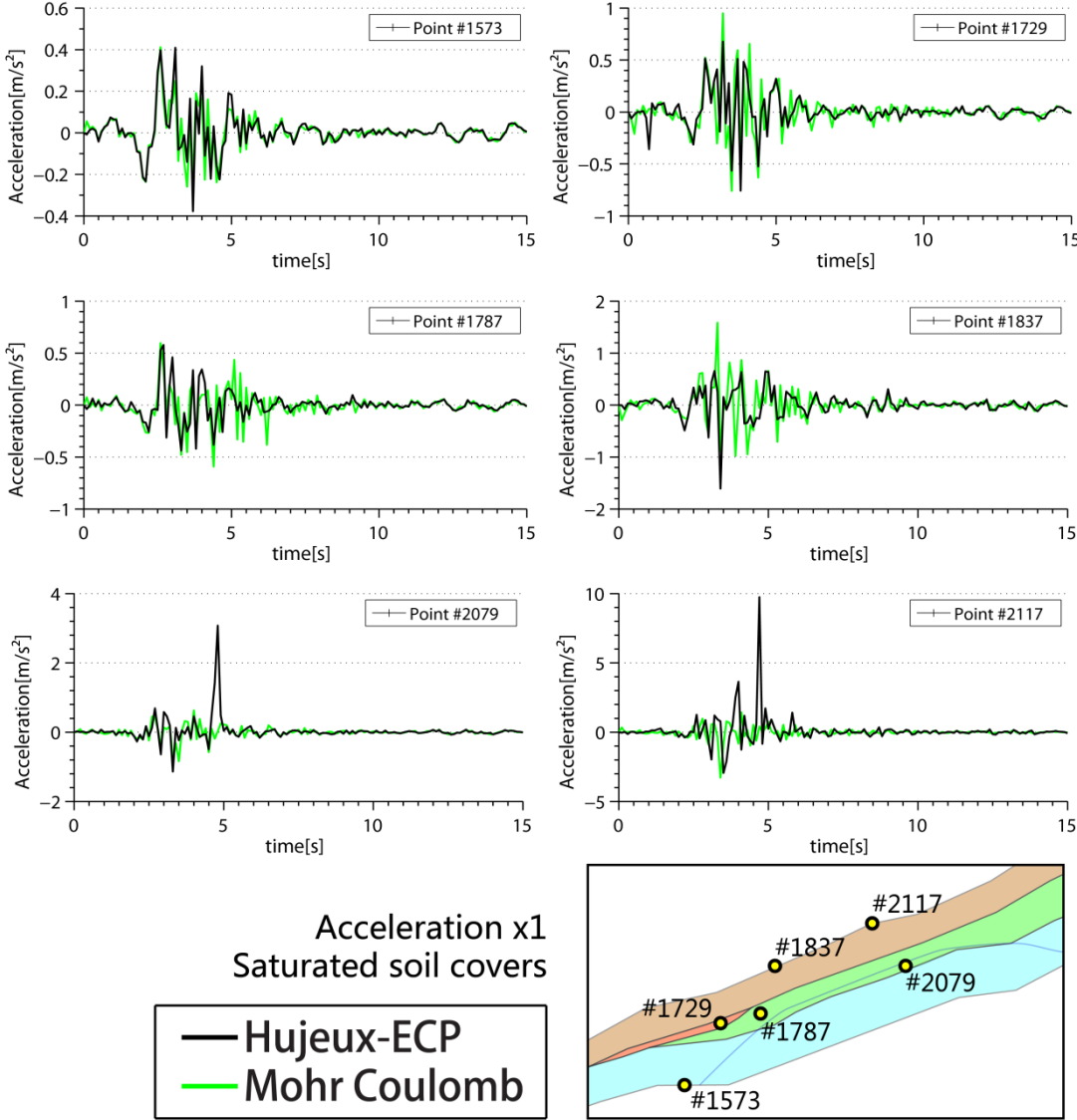


Figure 17: Variation of horizontal acceleration with time for two constitutive models, in the saturated case.

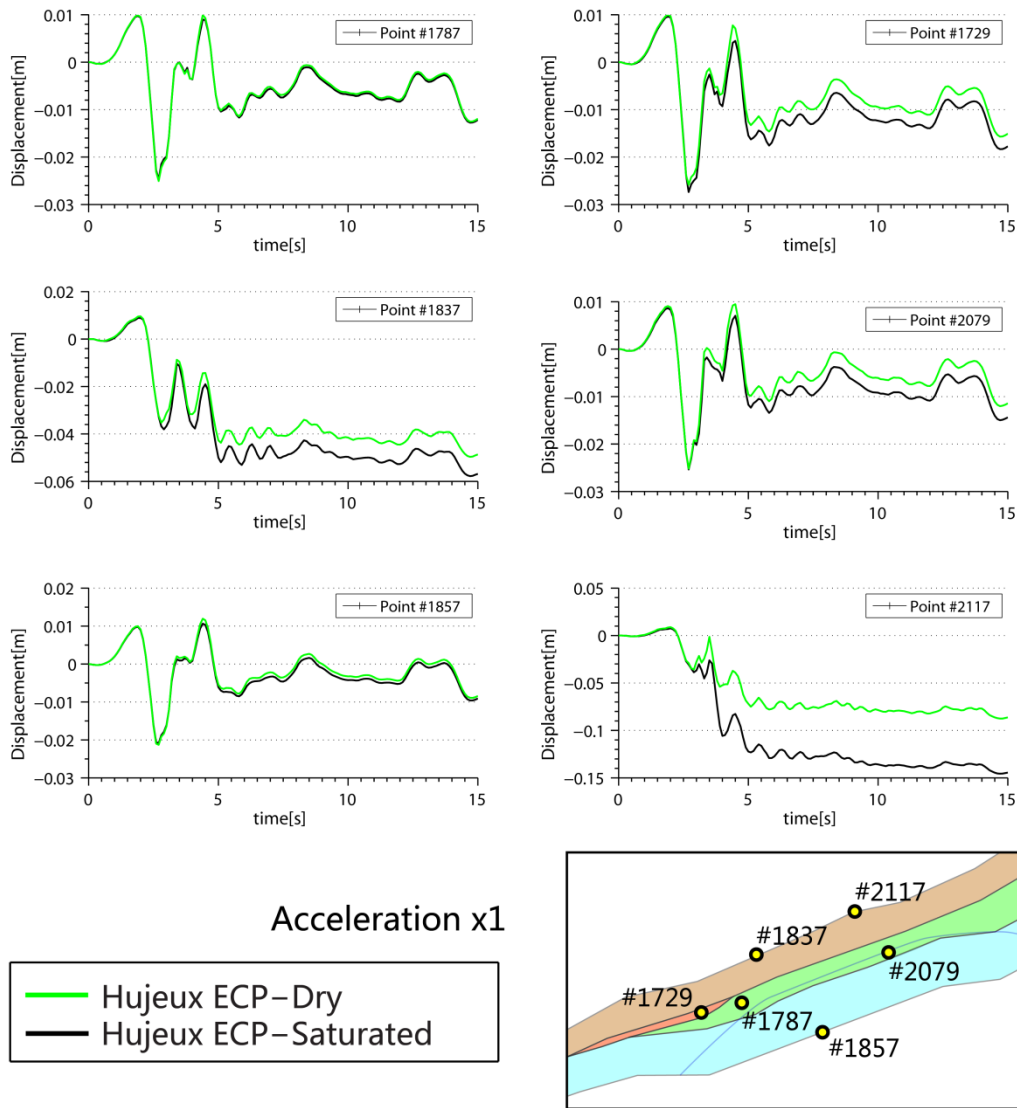


Figure 18: Variation of horizontal displacement with time at different nodes in terms of the sensibility of constitutive model and hydraulic model (input acceleration x1).

Figure 18 presents the numerical results obtained with two different hydraulic conditions. The importance of hydraulic conditions can be observed in comparison with the black line and the green one. One can notice that displacement at node #2117 in the saturated case is twice higher than that in the dry case, while a measurable difference is seen in most other soil locations. This is the location where maximum movements are observed (as shown in Figure 20). The movement of soil due to the cyclic loading compressed the soil, then the water is influenced and the inner pressure of water then increases in a proportional way to the level of displacement, which is then added to solid skeleton again. This process is the main cause of the significant level of displacement.

In general, displacements in the dry case are inferior to those in the saturated case because no pore water pressure is taken into consideration when the soil covers are assumed dry. The saturated model generates excess pore water pressure in the soil body, which decreases effective stress during the cyclic loading. Therefore, the soil loses much more of its resistance than that in the dry case. In addition, the formulation u-p considers the influence of the relative movement between the fluid and solid skeleton, which will cause supplementary movements when this formulation is applied to whole soil body.

The distribution of displacement 5 seconds after the beginning of the earthquake (Figure 19, dry case) shows that two different phenomena can be induced by the seism. As foreseen, most of the top layer of the steepest zone undergoes large displacements. But we can also observe that in the upper and less steep part of the landslide, displacement of the same magnitude are observed on larger volume of soil. Landslides scarp #1 and #3 show measurable displacements down to more than 10 m depth. More significantly, landslide scarp #2 extends to a large volume of soil and its shape is quite typical of shallow landslides. The maximum displacement in all those locations is the same, around 7 cm, which should be seen as an indicator of possible triggering.

This analysis can be compared with the one that can be done of the saturated case shown in Figure 20. Differences are seen mainly in the upper part of the landslide. On the surface, the locations of high displacements are the same. But the mechanisms that this figure shows are different. For the scarps #1 and #2, a change from a shallow sliding surface to a deep sliding surface is obvious. The surface under scarp #2 even reaches the low quality soil that was identified as an important factor in the non-dynamic behaviour of the landslide. This conjunction of facts, as well as the increase in total displacement simulated for that scarp (see Figure 18), should be interpreted as a much stronger indication of possible triggering, on a much larger volume of soil.

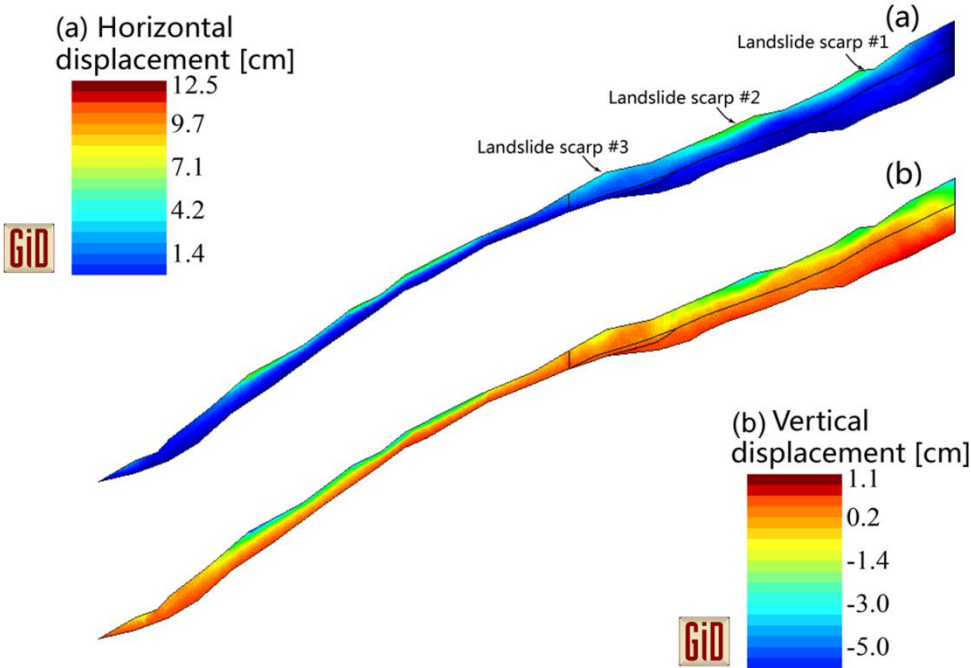


Figure 19: Distribution of (a) horizontal displacement and (b) vertical displacement in the dry case at t=5 s.

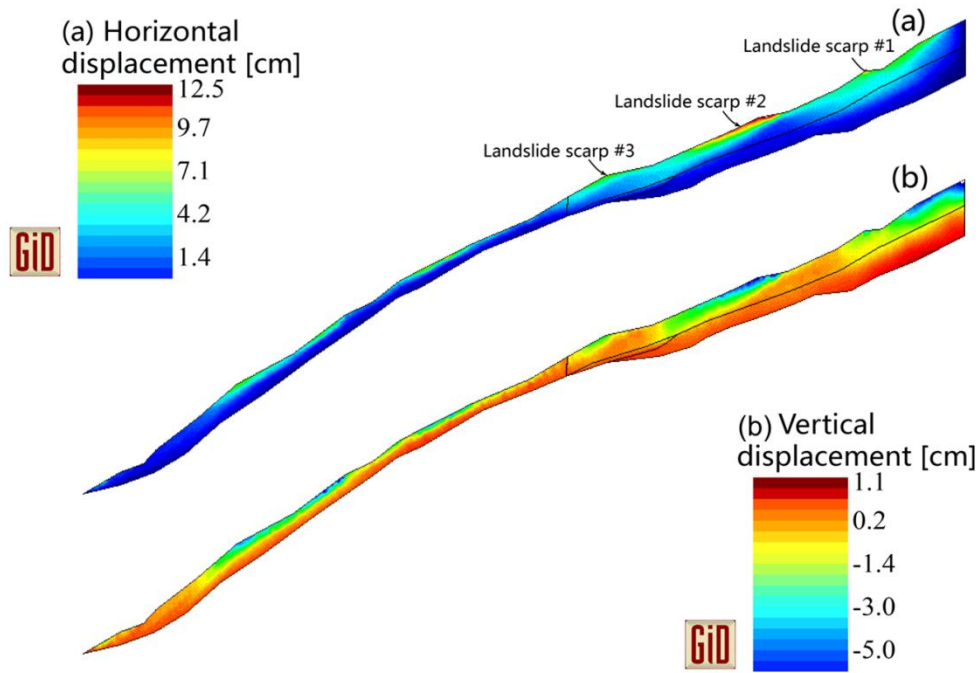


Figure 20: Distribution of (a) horizontal displacement and (b) vertical displacement in the saturated case at $t=5$ s.

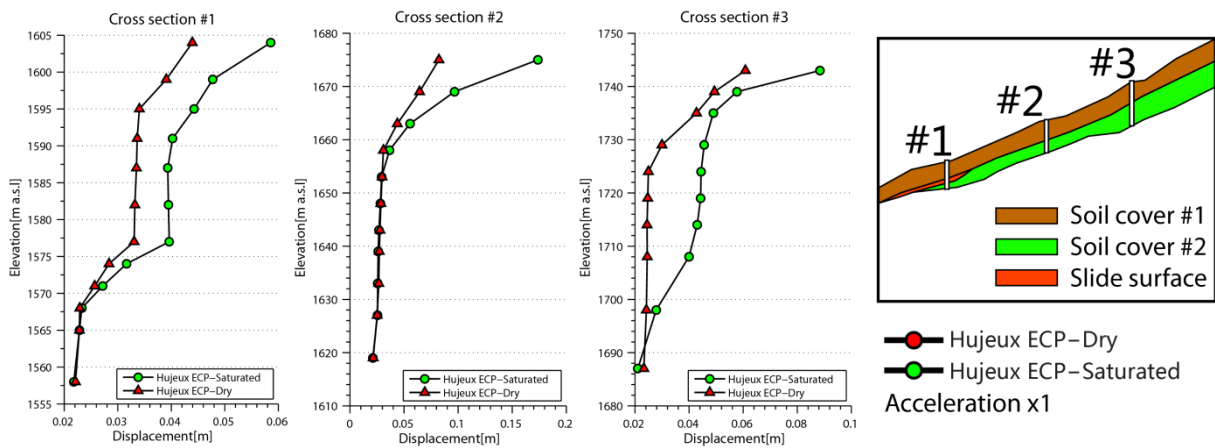


Figure 21: Maximum horizontal displacement profiles for three focus cross sections

Figure 21 shows the variation of peak displacements during seismic loading versus the elevation. Profile #1 crosses three materials and the other two cross two soil materials. The results shown for profile #1 show that the model reproduces well the characteristics of the sliding surface. This can be seen in the local increase in displacement between the elevations of about 1577 m a.s.l. and 1567 m a.s.l. where the slide surface is located. Due to its poor soil characteristics, the sliding surface contributes heavily in the global displacements observed in soil cover #1.

Using Hujieux-ECP model in the case of saturated soil, the upper surface slips more than the middle of soil covers. From 1595 m a.s.l. in profile #1 (1660 m a.s.l. in profile #2; 1735 m a.s.l. in profile #3), the horizontal movement extends quickly to the surface. This can be explained by the application of hydrology u-p formulation in the saturated case. Excess pore water pressure is developed throughout the model in this case by the almost undrained behaviour and by the plastic volumetric strains. Nevertheless, the initial effective stress (own weight) of the surface layer (about 10 meters thick in profile #1) is comparatively low and in the $p'-q$ plane, low shear resistance is found. Therefore the displacement increases in the superficial part of the soil body. The base of this shallow slip surface is

located between 5 and 15 m below the surface. Figure 20 shows that this behaviour is correlated with the presence of scarps in the profile, and that scarp #2 undergoes by far the largest displacement.

The problematic of soil liquefaction should be treated here also. This phenomenon can occur below the water table or in a saturated zone. In the case of *Les Peillettes*, the water table is situated just above the bedrock in which the main part of pore water pressure concentrates. However, the study focuses on the behaviour of soil subjected to an earthquake. The hydrostatic pore water pressure applied to the part of soil below the water table is low compared to the initial effective stress. In addition, even the total pore water pressure is not high enough to be higher than the effective stress. In the saturated case, the risk could be located in the higher part of the soil cover, but the nature of soil (weathered schist with blocks) renders the phenomenon improbable.

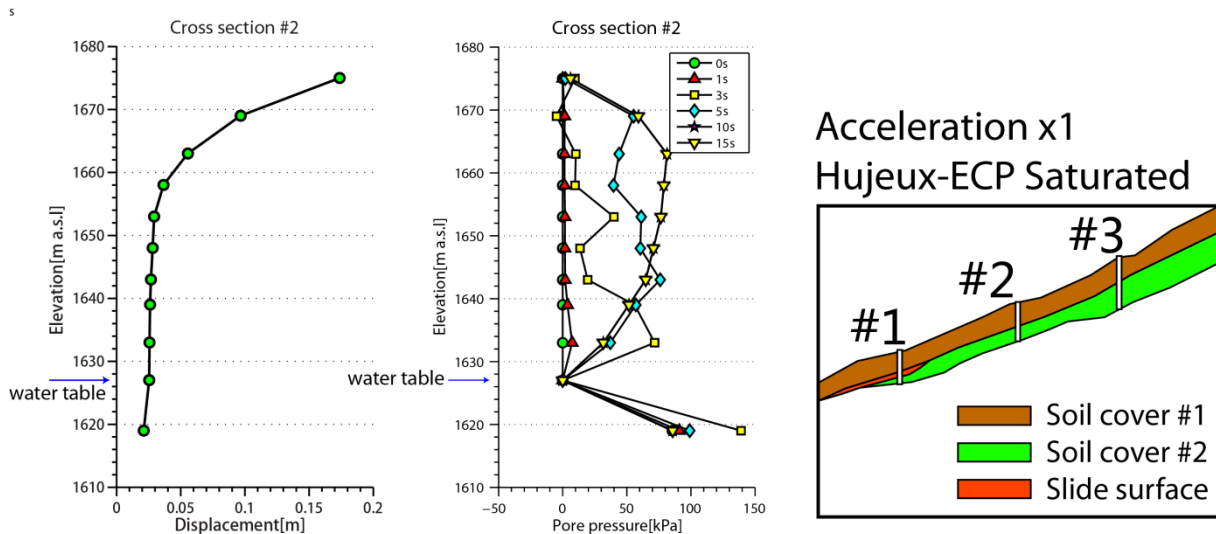


Figure 22: Maximum pore water pressure profile

Figure 22 establishes the magnitude of the excess pore pressures observed in the saturated case, and draws a comparison between a profile of these pressures and the observed displacements in the same profile. Be it above the water table (in infiltrating water) or under it (in steady-moving water), the excess pressure is less than 100 kPa. It can be noted that due to the way the water table is imposed, no excess pore pressures can be created at this precise location. Soil liquefaction risk can be estimated with the help of this graph. Only the first 5 metres, where vertical stress is lower than 100 kPa could be affected, but the nature of soil (weathered schist with blocks) renders the phenomenon improbable. While the magnitude of the excess pore pressures is not sufficient here to suggest liquefaction, it contributes to a significant decrease in effective stresses in the upmost part of the soil. This translates into a significant increase in displacements in the first 20 metres, compared to the lower part but also to the dry case (see Figure 21).

After the constitutive aspects were treated in the case study, the impact of the ground motion input is analysed. Figure 23 shows a general view of the horizontal ground accelerations obtained for some points of interest distributed in the considered zone (the related displacement responses are shown in Figure 25). Most acceleration peaks occurs less than 5 seconds after the beginning of earthquake. In the study of BRGM (2007) shown in Figure 24, oscillations continues until the end of computation time, because the soil is considered as a linear elastic behaviour and a rigid base assumption. Compared to their study, the simulations presented in this report are realistic in the sense that they significantly decrease at the end of earthquake, in the absence of horizontal wave reflections from site effect. This behaviour is due to the use of paraxial elements, which simulates radiation conditions at the base of finite element model in order to avoid the reflection of elastic waves in the interior of soil

body. In addition to these absorbent elements, material damping is introduced here through assumption of a non-linear constitutive law of soil.

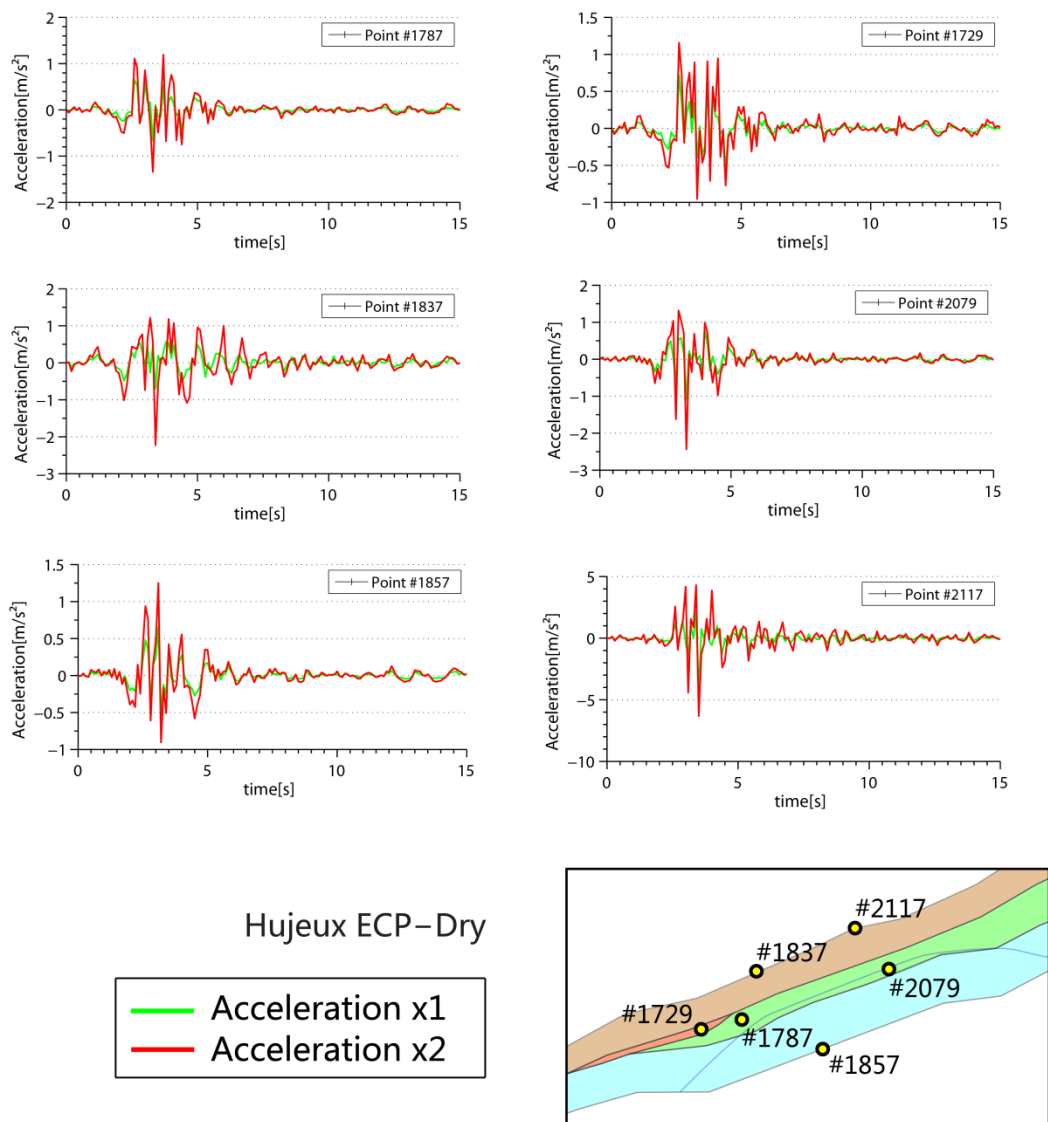


Figure 23: Variation of horizontal acceleration with time at different seism intensities, in the dry case.

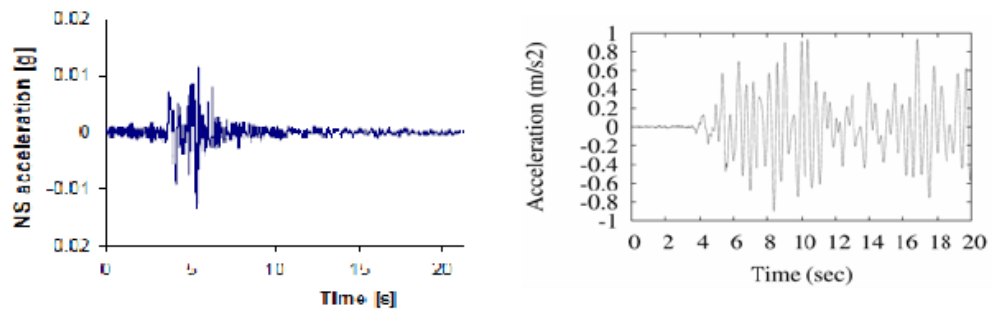


Figure 24: Input acceleration (left) and response of acceleration at one node (BRGM 2007)

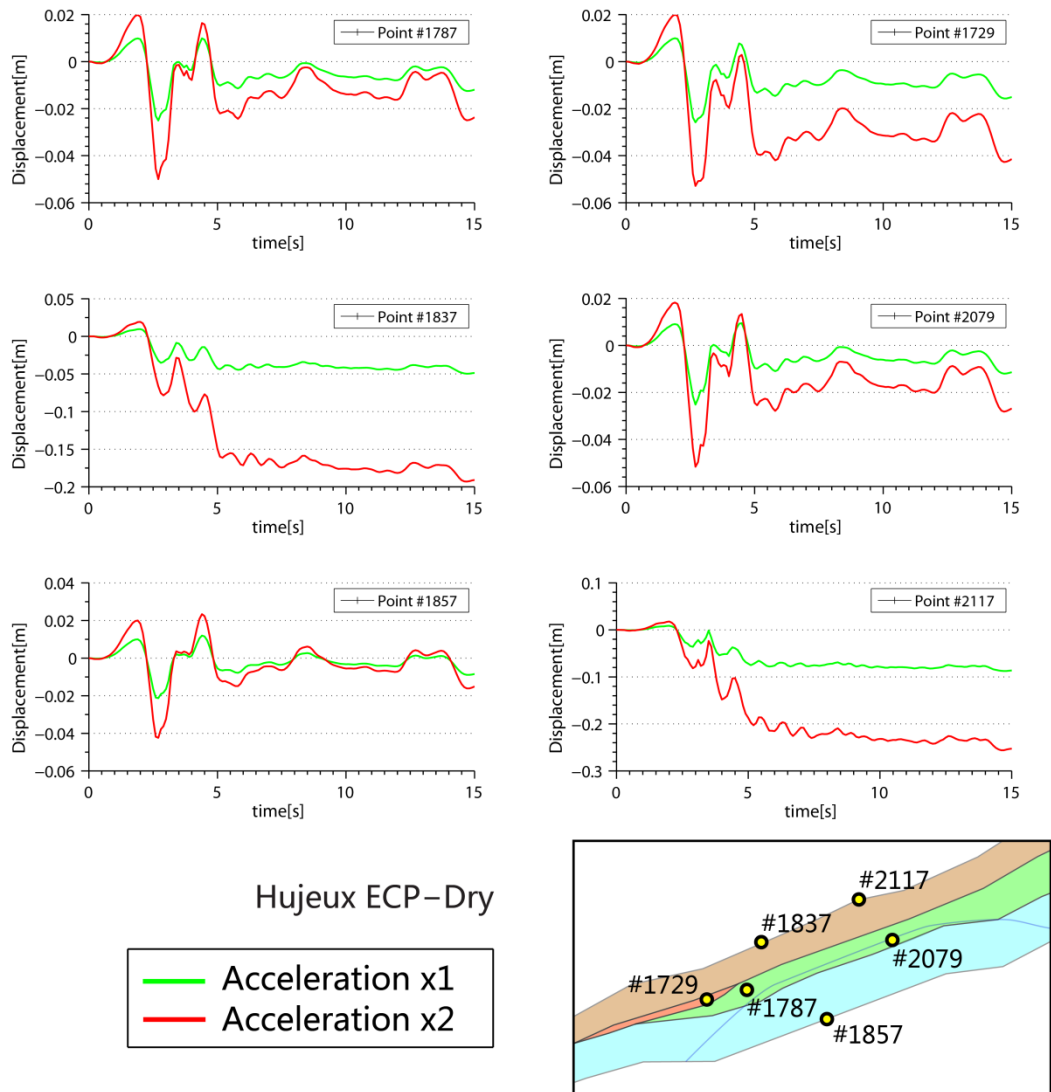


Figure 25: Variation of horizontal displacement with time at different seism intensities, in the dry case.

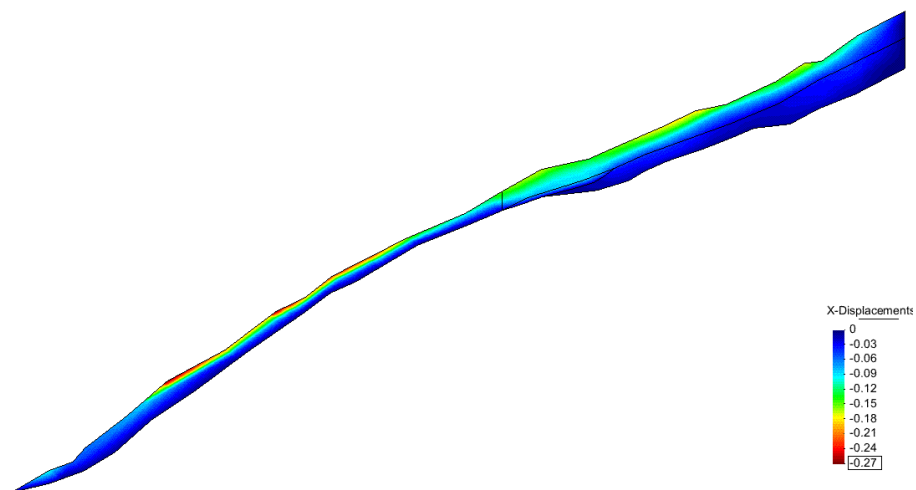


Figure 26: Distribution of horizontal displacement at $t=5$ s with doubled acceleration input.

The phenomenon of amplification in terms of acceleration is clear comparing the node #1537 and the node #1837 or the node #2117. The amplification ratio between the peak ground acceleration at the base and that at surface varies between 2 and 4 and is largely dependent on actual location. Comparing

the two cases of input acceleration, it appears that no strict linearity between input and output is found, but that PGA amplification ratio is not largely affected by higher amplitudes. It should be noted that in some nodes (#2117), more peaks are generated by the bigger acceleration input, which are responsible for the larger simulated displacements.

In Figure 25, variations of horizontal displacements with time are presented at different nodes. The analysis of these curves reveals that most of the permanent displacements appear in the first 5 seconds, in a single step. The maximum displacement at bedrock level is 2 cm in the base case, while the maximum displacement at node #2117 is a comparable 3 cm. The effect of non-linearities is observed in that permanent displacement at that point reaches 2.5 cm. The amplification effect observed in accelerations is not found as strongly in displacements. In the middle of soil cover (nodes #1787 and #2079), the shapes of displacement histories are nearly the same. Compared to node #1787, the nearby node #1729 in slide surface undergoes a larger displacement. The two points at the surface of slope #1837 and #2117 have more important permanent displacements than those in the soil body. Node #2117 is located just above a scarp, which is the main reason that it moves the most among these focus nodes.

These observations can be more clearly explained by the contour map shown in Figure 26 (scale is different from Figures 19 and 20). Yet another regime for the observed sliding is observed. In this higher intensity case, a deep and large movement of the upper part of the slope is found, with no obvious influence of the scarps. In the steeper part of the landslide, maximum displacements are observed, but the regime remains the same as in Figure 19.

Conclusion

The numerical study of a very varied, as well as hydrologically and geologically well-known, landslide has revealed many aspects that should be taken into account in the evaluation of possible triggering of a landslide during a seism. In the two dimensional study of the landslide *Les Peillettes*, an appropriate constitutive law Hujoux model is selected for numerical simulation, incorporating several aspects such as cyclic behaviour, dilatancy and kinematic hardening behaviour. In addition to this rheology relationship, a dynamic-based hydrology model is also used. Therefore the influence of pore fluid is taken into account on the behaviour of solid skeleton. Paraxial elements are used for the dynamic analysis, in order to avoid wave reflections on boundaries. The model is also used to analyse the combination of hazards that can lead to a saturated soil being subjected to a seism, after heavy rain or during snow melting period.

This finite element model is able to reveal various possible mechanisms of rupture for this landslide. Two families are identified: deep-seated slide surfaces and shallow localized slide surfaces under scarps. None of these surfaces are reaching the position of the water-table, which is an interesting conclusion, although water itself was found an important factor in the results. The magnitude of displacement, and therefore the probability of triggering, is largely influenced by the saturation state of the soil. The response of the landslide with an infiltrated soil, with low water pressures above the water table, is significantly more critical than the one obtained with dry soil. The magnitude of displacements in that case is two times the magnitude seen in the dry case. In the tested range, a stronger earthquake also commands a change in possible sliding regime. The advanced constitutive model and detailed finite element model was capable of exhibiting not only a proportioned response to the three cases, but a detailed view on all the secondary effects that important parameters (input, hydraulic state) can have on the response of a given site.

Two aspects could be treated to confirm the orientation of the conclusions of this study. The first part would be to run actual laboratory experiment on soil samples from the landslide. The second aspect would be to take into account an unsaturated soil behaviour to complete the explanation of the evolution between dry and saturated case and identifying a possible threshold in water conditions.

References

- Arvin, M. R., Askari, F. and Farzaneh, O. (2012). Seismic behavior of slopes by lower bound dynamic shakedown theory. *Computers and Geotechnics* **39**(0): 107-115.
- Aubry, D., Chouvet, D., Modaressi, A. and Modaressi, H. (1986). *Gefdyn software—Logiciel d'analyse du comportement mécanique des sols par éléments finis avec prise en compte du couplage sol-eau-air*. Chatenay-Malabry, France, LMSS-Mat, Ecole Centrale Paris.
- Aubry, D., Hujeux, J.-C., Lassoudière, F. and Meimon, Y. (1982). *A double memory model with multiple mechanisms for cyclic soil behaviour*. Proceedings International Symposium on Numerical Models in Geomechanics, Zürich, A. A. Balkema.
- Benzenati, I. and Modaressi, H. (1994). Paraxial approximation for poroelastic media. *Soil Dynamics and Earthquake Engineering* **13**(2): 117-129.
- Bianchetti, G. and Bagnoud, A. (1999). *Glissement des Peillettes : campagne de forages profonds (1997-98) : rapport géologique et hydrogéologique : commune de Grône*. Sion, Centre de recherche sur l'environnement alpin (CREALP).
- BRGM (2007). *Application of numerical models to case histories: Earthquake cases - Phase II*. Risk mitigation for earthquakes and landslides integrated project. LESSLOSS, Deliverable 96b.
- Cekerevac, C. (2003). *Thermal effects on the mechanical behaviour of saturated clays: an experimental and constitutive study*. PhD thesis at Laboratoire de mécanique des sols, École Polytechnique Fédérale de Lausanne.
- De Martin, F., Modaressi, H. and Aochi, H. (2007). Coupling of FDM and FEM in seismic wave propagation.
- Fäh, D. and COGEAR Working Group (2010). Coupled Seismogenic Geohazards in Alpine Region.
- Fifer Bizjak, K. and Zupančič, A. (2009). Site and laboratory investigation of the Slano blato landslide. *Engineering Geology* **105**(3-4): 171-185.
- Fritsche, S., Gisler, M., Schwarz, G., Fäh, D. and Kästli, P. (2010). Historical earthquakes in the Valais.
- Hujeux, J. C. (1985). Une loi de comportement pour le chargement cyclique des sols. *Génie Parasismique*, V. Davidivici (Ed.). Paris, Presses ENPC, 287-302.
- Kramer, S. L. (1996). *Geotechnical Earthquake Engineering*, International Series in Civil Engineering and Engineering Mechanics. New Jersey, Prentice-Hall.
- Laloui, L., Tacher, L., Moreni, M. and Bonnard, C. (2004). *Hydromechanical modeling of crises of large landslides : application to the La Frasse Landslide*. 9th International Symposium on Landslides, Rio de Janeiro, Brazil, Balkema.
- López-Caballero, F. (2003). *Influence du comportement non linéaire du sol sur les mouvements sismiques induits dans des géo-structures*. PhD thesis at Laboratoire des Mécanique des sols, Structures et Matériaux, Ecole central de Paris, France.
- Malet, J.-P. (2003). *Les glissement de type écoulement dans les marnes noires des Alpes du Sud. Morphologie, fonctionnement et modélisation hydro-mécanique*. PhD thesis at Ecole doctorale des sciences de la terre, de l'univers et de l'environnement, Institut de Physique du Globe, Université Louis Pasteur - Strasbourg I.
- Mellal, A. (1997). *Analyse des effets du comportement non linéaire des sols sur le mouvement sismique*. PhD thesis at Laboratoire des Mécanique des Sols, Structures et Matériaux, Ecole Centrale de Paris, France.

- Modaressi, A. (2003). *Modélisation des milieux poreux sous chargements complexes*. PhD thesis at LMSSMat, Ecole centrale de Paris.
- Modaressi, A., Stefania, S. and Luca, P. (2008). Influence of past loading history on the seismic response of earth dams. *Computers and Geotechnics* **35**(1): 61-85.
- Rascol, E. (2009). *Cyclic Properties of Sand: Dynamic Behaviour for Seismic Applications*. PhD thesis at Laboratoire de mécanique des sols, École Polytechnique Fédérale de Lausanne.
- Zienkiewicz, O. C., Leung, K. H. and Pastor, M. (1985). Simple model for transient soil loading in earthquake analysis. I. Basic model and its application. *International Journal for Numerical and Analytical Methods in Geomechanics* **9**(5): 453-476.
- Zienkiewicz, O. C. and Shiomi, T. (1984). Dynamic behaviour of saturated porous media; The generalized Biot formulation and its numerical solution. *International Journal for Numerical and Analytical Methods in Geomechanics* **8**(1): 71-96.